Geomechanics for Energy and the Environment 7 (2016) 26–46

Contents lists available at ScienceDirect

Geomechanics for Energy and the Environment

journal homepage: www.elsevier.com/locate/gete

Effect of CO_2-induced reactions on the mechanical behaviour of fractured wellbore cement

Timotheus K.T. Wolterbeek*, Suzanne J.T. Hangx, Christopher J. Spiers

HPT laboratory, Faculty of Geosciences, Utrecht University, Budapestlaan 4, 3584CD, Utrecht, The Netherlands

HIGHLIGHTS

- Base-line yield and failure criteria were constructed for unreacted wellbore cement.
- Fractured samples were subsequently reacted with CO_2-saturated water and re-tested.
- Reaction resulted in reappearance of a peak strength and higher frictional strength.
- These results suggest mechanical healing of the fractures over periods of months.
- This implies reaction-induced sealing is unlikely negated by mechanical weakening.

ARTICLE INFO

Article history:
Received 8 January 2016
Received in revised form 19 February 2016
Accepted 20 February 2016
Available online 8 March 2016

Keywords:
CO_2 storage
Wellbore integrity
Cement carbonation
Mechanical properties
Fracture healing
Failure

ABSTRACT

Geomechanical damage, such as fracturing of wellbore cement, can severely impact well integrity in CO_2 storage fields. Chemical reactions between the cement and CO_2-bearing fluids may subsequently alter the cement's mechanical properties, either enhancing or inhibiting damage accumulation during ongoing changes in wellbore temperature and stress-state. To evaluate the potential for such effects, we performed triaxial compression tests on Class G Portland cement, conducted at down-hole temperature (80 °C) and effective confining pressures ranging from 1 to 25 MPa. After deformation, samples displaying failure on localised shear fractures were reacted with CO_2–H_2O, and then subjected to a second triaxial test to assess changes in mechanical properties. Using results from the first phase of deformation, baseline yield and failure criteria were constructed for virgin cement. These delineate stress conditions where unreacted cement is most prone to dilatational (permeability-enhancing) failure. Once shear-fractures formed, later reaction with CO_2 did not produce further geomechanical weakening. Instead, after six weeks of batch reaction, we observed up to 83% recovery of peak-strength and increased frictional strength (15%–40%) in the post-failure regime, due to carbonate precipitation in the fractures. As such, our results suggest more or less complete mechanical healing on timescales of the order of months.

1. Introduction

Wellbores in subsurface reservoir systems are man-made fluid transport pathways intended for fluid exploration, production or injection. They are typically lined with a steel casing, the outside of which is sealed against the adjacent rock formations using Portland-based cement. Upon well abandonment, further cement is injected to form a sealing plug in the central bore. Despite these measures, wells are widely recognised as potential leakage pathways from geological systems targeted for storage of CO_2[1–3]. Even though cements tailored to be more resistant to acidic, CO_2-rich environments are being developed for the construction of new wells[4,5], many of the sites

---

* Corresponding author. Tel.: +31 0302535079.
E-mail address: t.k.t.wolterbeek@uu.nl (T.K.T. Wolterbeek).

http://dx.doi.org/10.1016/j.gete.2016.02.002

considered for geological storage of CO_2 include pre-existing (legacy) wells of only standard design, i.e. incorporating conventional Portland cements[6,7]. In these wells, the assumed barrier to unwanted fluid migration is provided by the cement seals, which in their virgin condition have a primary matrix permeability of 10^{-21} to 10^{-17} m^2[8,9].

While standard Portland cements readily degrade when reacted with large, free volumes of CO_2-bearing fluid[10,11], experiments employing lower fluid-to-solid ratios, representative of the conditions expected down-hole, suggest that the extent of reaction in situ will be limited and that reaction may even result in decreased cement porosity and permeability[12,13]. These findings are corroborated by field evidence, such as from the SACROC field[14] and Dakota Sandstone reservoir[15]. Here, despite decades of exposure to CO_2, cement samples retrieved from depth retained their integrity. On this basis, it seems unlikely that chemical degradation alone will impair cement integrity, and hence intact wellbore cement is usually assumed to form a reliable seal against CO_2 migration[16,17].

However, structural damage within the cement, or at the cement–casing and cement–rock interfaces, may change this picture, with defects such as fractures and interfacial debonding cracks or voids providing flow paths that can potentially enhance permeability. In recent years, numerous studies have investigated the effect of CO_2–H_2O–cement reactions on the transport properties of pre-fractured cement and cement containing simulated fractures[13,18–24]. These efforts have mainly addressed how alteration and carbonation, by permeating CO_2-bearing fluids, affect fracture permeability, fracture-wall chemistry and microstructure. By contrast, the effects of reaction on the mechanical properties of wellbore cement under in situ PT conditions[25–29] have received relatively little attention[17]. Yet, significant stress changes will occur in the well system during CO_2 injection and long-term storage, inevitably causing some damage[30–32]. Therefore, to assess well integrity confidently, it is important to investigate coupled chemical–mechanical effects. Of specific importance here is the effect of CO_2–H_2O–cement reactions on the mechanical strength of already fractured cement. If chemical reaction between fracture walls and CO_2-bearing fluid results in frictional or cohesive weakening of the fractures, this will facilitate reactivation, growth and (re)opening during ongoing changes in storage system temperature and stress state. Leakage pathways for CO_2 could then be maintained open dynamically. On the other hand, fracture sealing (i.e. permeability reduction), due to carbonate cementation[13,21,22] or asperity-weakening[19,23,33], may be accompanied by fracture healing (i.e. mechanical strength recovery), impeding such fracture reactivation and leakage.

To resolve which effect dominates, we report experiments on the impact of CO_2-induced reactions on the mechanical properties of fractured wellbore cement. We performed conventional triaxial compression tests on cylindrical samples of API-ISO Class G HSR Portland cement at a temperature (T) of 80 °C, confining pressures (P_c) ranging from 6 to 30 MPa, and a pore fluid pressure (P_f) of 5 MPa ($P_c^{eff} = 1$ to 25 MPa). This temperature was chosen to be similar to down-hole, while the effective confining pressures were chosen to promote cement fracturing, hence "worst-case behaviour" in a well. Selected, shear-fractured cement samples were subsequently exposed to CO_2-saturated water under hydrostatic conditions ($T = 80$ °C, $P_f = \sim 12$ MPa) for a period of six weeks. After CO_2-exposure, the samples were subjected to a second triaxial compression test, at the original conditions, to evaluate the effects of reaction on fracture strength. We apply a variety of yield and strength parameters and envelopes to quantify the strength of both the unreacted and reacted samples. The results show that static reaction leads to significant mechanical strengthening (healing) of fractured wellbore cement.

2. Experimental methods

2.1. Sample preparation and porosity determination

The present experiments were performed on cylindrical samples of API-ISO Class G HSR Portland cement. This is one of the most widely used well-cementing materials[34] and is considered to be an effective sealing agent at well temperatures up to ∼110 °C[35]. Cement slurry was prepared from commercially obtained clinker (Dyckerhoff AG, Lengerich), in accordance with ISO 10426-2 practice (API Recommended Practice 10B-2), using deionised water at a water-to-cement ratio of 0.44 (ISO 10426-1; API Specification 10A). After mixing, the cement slurry was slowly poured into cylindrical moulds measuring 90 mm length and 35 mm diameter. Extraction of air from the slurry was promoted by ultrasonically vibrating the moulds for 5 min, followed by degassing under vacuum for 15 min. The moulds were subsequently placed in a water-filled thermobath, maintained at 60 °C ± 0.2 °C, where the cement was allowed to cure under lab air, i.e. at atmospheric pressure, for three days. The hardened cylindrical cement samples were then removed from their moulds and cured further at room temperature in closely fitting, airtight, water-filled containers, to avoid long-term exposure to atmospheric CO_2. On the basis of curing time, two groups of samples were obtained, namely "immature cement" (tested after 21 days curing) and "mature cement" (tested after >6 months curing). Prior to triaxial testing, the fluid-saturated samples were removed from their containers, then cut and ground square at the ends to obtain right cylinders of 75 ± 1 mm length and 35 mm diameter. The samples were subsequently returned to and kept in their water-filled curing containers until use.

The sample porosity with respect to water (40.1% ± 1.2% for mature cement samples) was determined from weight loss data obtained by drying initially water-saturated samples at 105 °C until a constant weight was attained. Note that this method, although widely adopted[36–38], typically overestimates the actual porosity, as some chemically bound water is inevitably lost, though generally not accounted for[36].

2.2. Triaxial testing apparatus

Conventional compression experiments were performed in an externally heated, triaxial compression apparatus (Fig. 1), described in detail by Peach[39], Peach and

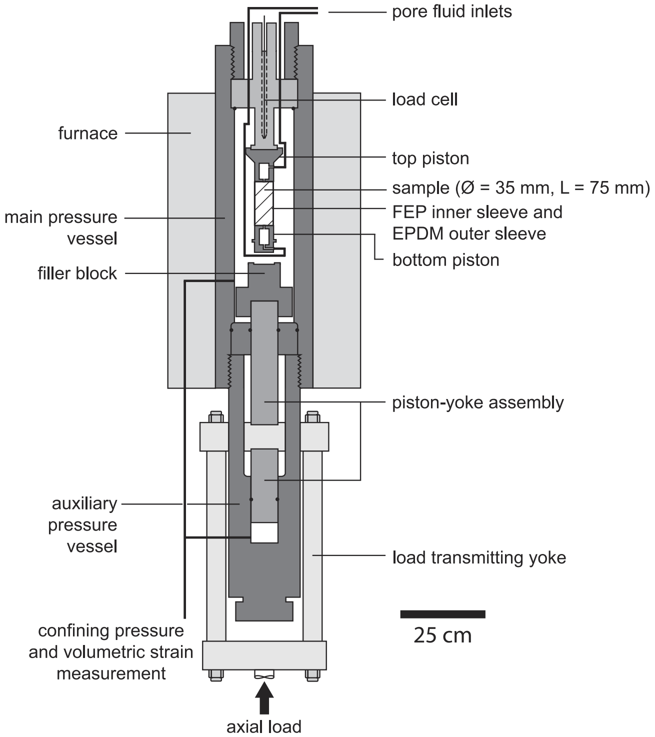

Fig. 1. Schematic diagram (scale approximate) of the triaxial compression apparatus used in our experiments, showing the internal details of the machine (modified after Hangx et al.[41]).

Spiers[40] and Hangx et al.[41]. It consists of a main pressure vessel containing the sample, a pressure-compensating auxiliary vessel, and a load transmitting piston–yoke assembly driven by a motor plus gearbox and ball screw system. As the piston–yoke assembly is advanced to load the sample, silicone oil is displaced from the main to the auxiliary pressure vessel, maintaining a nominally constant system volume. Dynamic and static sealing are achieved using Viton O-rings.

In this system, sample volume changes are derived from the piston displacement of a servo-controlled pump (resolution ±20 μl), used to maintain a constant confining (silicone oil) pressure (P_c). Confining pressure is measured using a pressure transducer (100 MPa range, resolution ±0.02 MPa) located close to the main pressure vessel. Axial load on the sample is measured using a semi-internal, differential variable reluctance transformer-based load cell, located at the top of the vessel (400 kN range, resolution ±0.035 kN). Piston displacement is measured externally using a linear variable differential transformer (100 mm range, resolution ±0.8 μm). Two Inconel-sheathed, K-type thermocouples, brought into the main pressure vessel through a port in the load cell block, are used to measure temperature at the sample surface. Temperature is controlled using a proportional–integral–derivative process controller (400 °C range, resolution ± 0.02 °C) equipped with a K-type control thermocouple, positioned in the windings of the external furnace. Pore fluid pressure (P_f) is applied via inlets at the top and bottom ends of the sample assembly and controlled using a second, servo-controlled, volumetric pump (resolution ±20 μl). Pore fluid volume changes (ΔV_p) are measured using a linear potentiometer, which records the piston displacement of this second pump. Pore fluid pressure is measured using a pressure transducer (50 MPa range, resolution ± 0.02 MPa), located just outside the main pressure vessel.

2.3. Sample assembly

For initial triaxial testing, fluid-saturated cylindrical samples of virgin cement were removed from the curing containers and located between top and bottom steel end-pistons (Fig. 1). To reduce friction between the sample and the pistons, thin (50 μm), perforated (hence permeable) Polytetrafluoroethylene (PTFE) sheets were included in the interfaces. The assembly was then rapidly jacketed using a tightly-fitting Fluorinated Ethylene Propylene (FEP) inner sleeve, of the same length as the sample, and covered using a longer, outer sleeve of Ethylene Propylene Diene Monomer (EPDM) rubber. Finally, the outer sleeve was sealed against the top and bottom end-pistons using wire tourniquets, to produce the completed assembly. The pore fluid reservoir and bore in each of the end-pistons (Fig. 1) were then primed with curing fluid from the sample container.

2.4. Initial triaxial testing procedure

In setting up each first-phase deformation test, the sample assembly plus load cell were placed in the oil-filled main pressure vessel (Fig. 1). The vessel was then sealed and the sample connected to the pore fluid pressure system. After applying a small confining pressure ($P_c \approx$ 1–2 MPa), the pore fluid system was rapidly vacuum-saturated with water. Subsequently, the confining and pore fluid pressures were increased simultaneously, keeping the confining pressure slightly higher than the pore fluid pressure, until the pore fluid pressure reached the target value for the experiment. The system was then heated to the required temperature at constant pore fluid pressure, while maintaining the confining pressure above the pore fluid pressure and close to, but below, the target value for the deformation experiment. A stable temperature of ~80 °C was generally reached within 5 h. At this temperature, the confining pressure was adjusted to the desired test value. Prior to deformation testing, the system was left for 1–2 h to reach thermal and pressure (P_c, P_f) equilibrium.

Initial deformation was then started by advancing the piston–yoke assembly (Fig. 1) at a constant displacement rate, corresponding to a nearly constant strain rate of $\sim 10^{-5}$ s^{-1}, thereby increasing the axial load on the sample. Each run was completed by arresting the piston and then reversing the drive motor, removing the applied load to a small residual value determined by the dynamic seal friction. If a peak-stress occurred, the sample was assumed to have failed in a localised, brittle manner. In these tests, the sample was immediately subjected to a second loading cycle to measure the post-failure properties (frictional strength) of the fractures formed. Experiments were then terminated by releasing the pore fluid pressure, hydraulically retracting the piston–yoke assembly, removing the confining pressure and cooling to room temperature, after which the sample was extracted from the machine.

The complete set of experiments performed is listed in Table 1. In addition to the triaxial tests on immature and mature cement, two purely hydrostatic compaction experiments were performed on mature cement samples (preparation, assembly and system equilibration as above). The first hydrostatic experiment (A-HS1) was conducted at a constant temperature of 80 °C, a pore fluid pressure (P_f) of 5 MPa, and an initial confining pressure (P_c) of 6 MPa, which was subsequently ramped up at ~30 MPa h^{-1} to a final P_c of 59 MPa. In the second hydrostatic test (A-HS2), P_c was instead increased at a rate of ~3 MPa h^{-1}, employing a mid-test hold for 13 h before resuming loading. The aim of these experiments was to constrain the hydrostatic stress required to cause pore collapse, and to investigate potential loading rate or creep effects. No hydrostatic compaction tests were performed on the immature cement samples.

2.5. Data acquisition and processing

A PC plus 16-bit National Instruments VI logger system was used to log the internal axial load, piston displacement, confining pressure, sample temperature, system volume change, pore fluid pressure and pore fluid volume change signals every 0.2 s throughout the deformation experiments. The data obtained were processed to yield differential stress (σ_1–σ_3), axial engineering strain (e), true axial strain rate ($\dot{\varepsilon}$), volumetric strain (e_V) and pore volume change (ΔV_p) data versus time, thus enabling stress–strain curves to be generated. All displacement and volume change data were corrected for apparatus distortion using predetermined stiffness calibrations. Sample volume and pore fluid volume changes were similarly corrected for thermal effects. Fractional pore volume change ($\Delta V_{p\%} = \Delta V_p/V_{p0}$) was determined from the initial pore volume (V_{p0}), which was itself obtained from the cement sample volume, assuming an initial porosity of 40.1% for all samples (see Section 2.1).

2.6. Batch reaction and fracture-reactivation experiments

Batch reaction experiments on selected, shear-fractured samples of mature cement only (A010, A050a and A050c) were performed for six weeks, using either water and CO_2 (R-A010, R-A050a) or water and argon (control experiment R-A050c), prior to a second triaxial compression (fracture reactivation) test. Sample preparation for reaction consisted of carefully removing the EPDM outer sleeve from the sample after deformation. Subsequently, the sample ends were sealed against the FEP inner sleeve using PTFE caps, cemented over the FEP using Loctite Blue silicone sealant. Slots were then cut in the tight FEP sleeve at the locations of distinct shear-fractures in the cement samples, to allow access of reactive fluid into to the fractured zones of the samples.

The samples were then individually placed in closely-fitting batch reactor pressure vessels[42], along with about 30 ml of demineralised water, which fully submerged the cement sample (fluid-to-solid volume ratio of 0.4–0.5). Following evacuation to remove air, the vessels were pressurised with either argon (non-reactive, control experiment) or CO_2 (reaction experiments) at room temperature. Subsequently, each vessel was isolated from the Ar or CO_2 supply and heated in a thermobath to a temperature of 80 °C, producing an initial total pressure of 14 MPa. Over the course of reaction, the pressure remained constant to within 5 MPa. The reaction experiments were terminated by depressurising (venting) the reactor vessels over a period of 3–6 h, while cooling to room temperature.

In preparation for the second series of triaxial tests, the PTFE caps and Loctite Blue sealant were carefully removed, the ends of the sample were repolished to again obtain right cylinders, and a new outer EPDM sleeve was applied. Triaxial testing was then repeated using the same procedure as described above for the unreacted, initially intact material, and using the same P_c, P_f, P_c^{eff} and T as in the first phase of triaxial testing. For this second triaxial testing phase, the pore fluid reservoir and bore in each of the end-pistons (Fig. 1) were primed with water.

2.7. Microstructural and chemical analyses

Microstructural analysis was performed on the unreacted and deformed samples (i.e. those subjected to the first phase of triaxial testing only), and on the deformed, reacted and re-deformed samples. To prepare the samples for microstructural analysis, the outer and inner polymer sleeves were carefully cut off, after which the samples were allowed to dry in an oven at 60 °C

Table 1
Summary of the experiments performed. All tests were conducted at a temperature of 80 °C and a pore fluid pressure (P_f) of 5 MPa. All triaxial tests were loaded axially at a constant displacement rate, corresponding to a near-constant strain rate of 10^{-5} s^{-1}. The two hydrostatic loading experiments were performed at the indicated rates.

Experiment sample code (test details)	P_c^{eff} (MPa)	σ_y (MPa)	σ_{max}(MPa)	P^*or C^* (MPa)	$\sigma_{1\%}$(MPa)	$\sigma_{2\%}$(MPa)	E_a(GPa)
Triaxial experiments on immature cement							
Y025a	2.5	20.1	33.2	9.0**	33.1	29.7	7.1
Y025b	2.5	20.0	34.8	9.2	–	30.3	7.4
Y050a	5	19.5	34.9	–	33.4	33.2	7.0
Y050b	5	27.3	39.2	12.5	34.9	32.3	6.5
Y075	7.5	21.4	38.4*	11.3**	38.3	39.0	7.1
Y100	10	19.1	38.6	15.9**	37.3	35.4	7.7
Y150	15	18.3	SH	19.3	35.0	39.7	5.9
Y200	20	22.4	SH	23.8	39.4	44.7	5.2
Y250	25	14.3	SH	29.1	35.0	41.2	6.1
Hydrostatic compression experiments on mature cement							
A-HS1 (rate 30 MPa h^{-1})	1–59	–	–	33.2	–	–	–
A-HS2 (rate 3 MPa h^{-1})	1–46	–	–	∼6	–	–	–
Triaxial experiments on mature cement							
A010	1	31.5	44.8	12.4	44.4	15.9	6.2
A025a	2.5	28.6	53.8	13.0	50.7	39.3	8.3
A025b	2.5	29.0	45.4	9.1	45.4	41.5	8.8
A050a	5	28.9	53.2	12.4	52.2	48.4	8.0
A050b	5	28.6	54.0	12.5	51.0	53.0	8.1
A050c	5	31.1	55.9	10.0	50.9	54.4	8.0
A100	10	25.0	60.3	15.3	47.9	58.4	8.9
A150	15	25.9	SH	20.6	48.0	57.5	7.1
A200	20	18.9	SH	24.0	40.8	48.1	7.4
A250	25	18.8	SH	30.0	42.2	55.1	7.1
Triaxial experiments on reacted cement (R-series, fracture reactivation experiments)							
R-A010 (6 weeks CO_2)	1	–	21.5	–	–	–	4.9
R-A050a (6 weeks CO_2)	5	–	43.9	–	–	–	6.4
R-A050c (6 weeks Ar)	5	–	38.4***	–	–	–	5.3

P_c^{eff} denotes effective confining pressure, σ_y and σ_{max} denote yield and peak strength, respectively. P^* and C^* denote critical stresses for hydrostatic and shear-enhanced compaction, respectively, while $\sigma_{1\%}$ and $\sigma_{2\%}$ are the differential stresses supported at 1% and 2% axial strain, respectively. E_a denotes apparent Young's modulus. SH denotes samples showing strain hardening with no peak-stress..

[*] Local maximum in differential stress followed by strain softening, but later followed by strain hardening, where the sample supports larger differential stresses.

[**] Should be considered as approximate only, due to uncertainty related to thermal effects.

[***] Apparent maximum related to subsequent strain weakening, not representing loss of cohesion.

for four weeks. This temperature was chosen, following Yurtdas et al.[43], to minimise the effects of microcrack formation and ettringite dehydration. After drying, the samples were impregnated with blue-dyed epoxy resin and subsequently sectioned axially, to produce whole-sample (thin-)sections. Shear fractured samples were sectioned approximately perpendicular to the main fractures present. The sections were studied optically, as well as using a Philips XL30FEG Scanning Electron Microscope equipped with Energy-Dispersive X-ray spectroscope (SEM-EDX) and an Edax Orbis PC Micro-XRF Spectrometer (μXRF). In addition, selected phases were investigated via X-ray Diffraction (XRD) analysis.

3. Results

3.1. Mechanical data

In the following, compressive stresses, compressive axial strains (e) and dilatant volumetric strains (e_V) are taken as positive. The principal compressive stresses are denoted as σ_i, with $\sigma_1 > \sigma_2 = \sigma_3 = P_c$ in our conventional triaxial experiments. We define the effective confining pressure as $P_c^{eff} = P_c - P_f$[44], and the effective mean stress as $P = (\sigma_1 + \sigma_2 + \sigma_3)/3 - P_f$. Peak-strength ($\sigma_{max}$) is defined as the maximum differential stress ($\sigma_1 - \sigma_3$) supported by the sample. The term 'failure' is used to describe loss of strength beyond the peak-strength, regardless of whether this is due to abrupt brittle fracturing or more gradual strain softening. For individual samples, the apparent Young's modulus (E_a) was determined from the initial quasi-linear portion of the differential stress versus axial strain curves, and the yield strength (σ_y) was taken as the differential stress at the upper bound of this linear portion[45]. The differential stresses supported by all samples at 1% and 2% axial strain ($\sigma_{1\%}$ and $\sigma_{2\%}$, respectively) were also employed as measures of strength. For mature cement tested in purely hydrostatic compaction mode, we additionally report the critical pressure (P^*, following Wong and Baud[46]) at which hydrostatic deformation becomes inelastic (i.e. non-linear). For the immature cement samples, P^* was not determined. The key mechanical data for all experiments are listed in Table 1.

3.1.1. Data for immature cement

Representative differential stress and volumetric strain versus axial strain data obtained during tests on immature

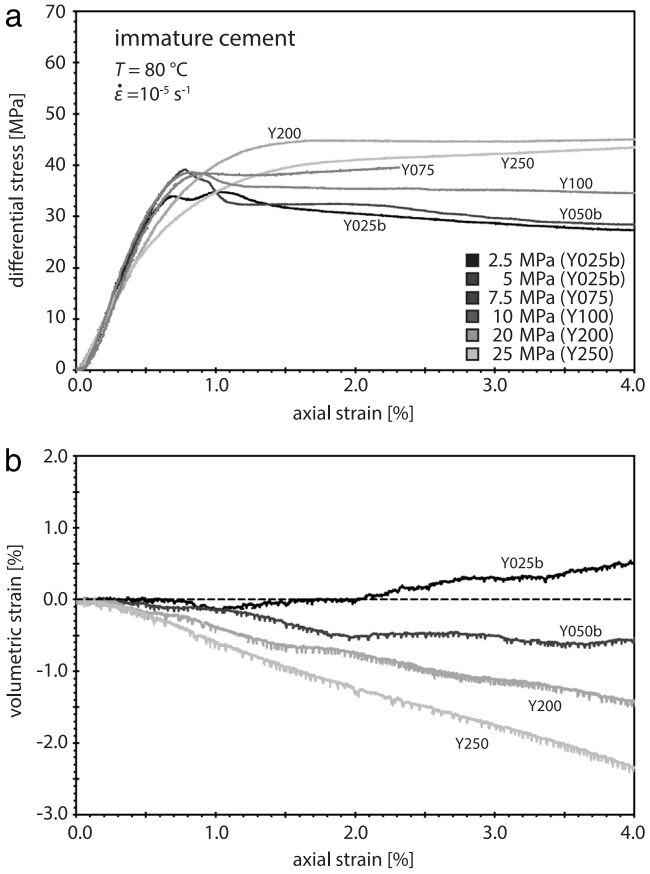

Fig. 2. (a) Differential stress and (b) volumetric strain versus axial strain curves for representative experiments on wet, immature cement. Greyscale indicates effective confining pressure, where sample codes relate to Table 1 (numbers in sample codes denote effective confining pressure in bar). Experiments Y025a, Y050a and Y150, showing similar behaviour, are not figured for readability.

cement (cured for 21 days) are plotted in Fig. 2. As seen in Fig. 2(a) (see also Table 1), all samples showed initial quasi-elastic loading behaviour. At low P_c^{eff} (2.5 to 5 MPa), this was followed by yielding at approximately 20 MPa and failure at differential stresses of approximately 35–40 MPa, with subsequent gradual strain softening beyond the yield point. At intermediate effective confining pressures (5 to 15 MPa), the observed behaviour was transitional between strain-softening and strain-hardening. At higher P_c^{eff} (15 to 25 MPa), no peak in strength occurred. Instead, after yielding at around 12–14 MPa, strain neutral to strain hardening behaviour was observed. The apparent Young's modulus varied from 5.2 to 7.7 GPa, where the lowest values were obtained in tests conducted at high confining pressure.

Volumetric strain (e_V) versus axial strain (e) curves for immature cement (Fig. 2(b)) showed continuous compaction in all experiments, except in the test conducted at the lowest effective confining pressure (2.5 MPa). In that experiment, minor compaction occurred in the first 1% of axial strain, with the minimum in volumetric strain (i.e. maximum compaction) roughly coinciding with the peak in sample strength, followed by dilatation at larger axial strains. No volumetric strain data are available for experiments Y025a, Y050a, Y075 and Y100, as these data could not be reliably corrected for thermal effects.

3.1.2. *Data for mature cement*

Fig. 3 shows representative differential stress and volumetric strain versus axial strain data obtained from the experiments on mature cement (cured for >6 months). The general behaviour is similar to that seen in the experiments on immature cement, with initial quasi-linear elastic behaviour being followed either by a peak-strength plus brittle stress-drop or strain-softening, or else by continuous strain-hardening (Fig. 3(a)). At the lowest P_c^{eff} investigated (sample A010, 1 MPa), yield occurred at approximately 31.5 MPa and 0.7% axial strain. This was followed by strain hardening towards a peak-strength of 44.8 MPa, reached at about 1% strain, and then by sudden failure. A near-constant residual strength of 15 MPa was attained from approximately 2% axial strain. At higher but still low P_c^{eff} (2.5 to 5 MPa), yielding occurred at about 0.5% axial strain and slightly lower stress ($\sigma_y = 20$ to 29 MPa), prior to attaining a peak-strength ($\sigma_{\max}$) of 46–54 MPa, reached at ∼1.3% axial strain, followed by more gradual strain softening (cf. A025a and A025b in Fig. 3(a)). Note that

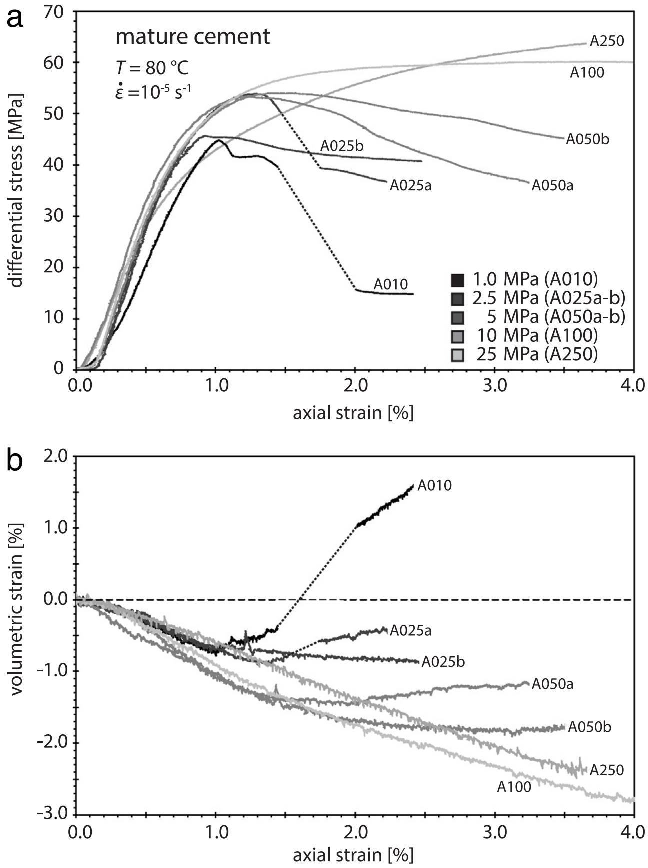

Fig. 3. (a) Differential stress and (b) volumetric strain versus axial strain data for representative experiments on wet, mature cement. Differential stress and volumetric strain are interpolated linearly where changes in stress and volume were too rapid to measure (dotted lines). Greyscale indicates effective confining pressure, where sample codes relate to Table 1 (numbers in sample codes denote effective confining pressure in bar). Experiments A50c, A150 and A200, showing similar behaviour, are not figured for readability.

yield and failure in experiment A025a ($P_c^{eff} = 2.5$ MPa) occurred at $\sigma_y = 20.1$ MPa (0.4% axial strain) and at $\sigma_{\max} = 53.8$ MPa (1.3% axial strain) with failure being followed by a marked stress-drop, similar to that exhibited by sample A010 ($P_c^{eff} = 1$ MPa). At higher P_c^{eff} (10 to 25 MPa), yielding occurred at even lower stress ($\sigma_y = 14$ to 22 MPa), as seen in the immature cement tests, and was followed by near-continuous strain hardening behaviour. Over the range of confining pressures investigated, the apparent Young's modulus varied between 6.1 to 8.9 GPa, with the obtained data crudely delineating a decreasing trend with increasing effective confining pressure (see Table 1), with the exception of sample A010 ($P_c^{eff} = 1$ MPa), which showed a comparatively low apparent Young's modulus.

Volumetric strain versus axial strain curves for the mature cement samples showed compaction in all experiments for the first ~1% of axial strain (Fig. 3(b)). However, a transition from compactant to dilatant behaviour is seen at low P_c^{eff} (1 to 5 MPa, see experiments A010, A025a, A50a — Fig. 3(b)), roughly at the axial strain where peak-strength is achieved. At the lowest P_c^{eff} (1 MPa), sample dilatation produced a net volume increase. At higher P_c^{eff} (10 to 25 MPa), the data show continuous compaction with increasing axial strain, though at a gradually decreasing rate.

3.1.3. Behaviour of the fractured and reacted samples

Immediately after initial deformation (shown in Fig. 3 and reproduced in Fig. 4), fractured samples A010, A050a and A050c were unloaded and reloaded to evaluate their post-failure reloading behaviour (Fig. 4). As described in Section 2.6, these samples were then reacted for six weeks and subsequently re-deformed (R-series triaxial tests, see end Table 1) in an attempt to reactivate the presumably altered fractures. Fig. 4 shows differential stress versus cumulative axial displacement (sum of displacements measured in all deformation stages) for both the pre- and post-reaction stages of these experiments. Reloading before reaction showed quasi-elastic behaviour, with minor decrease in sample stiffness, followed by a continuation of the strain-softening or strain-neutral behaviour seen at the end of the initial loading (Fig. 4). Upon reloading after the reaction stage, all samples again exhibited quasi-elastic behaviour, similar to that observed prior to reaction. Exposure of samples to water and argon (R-A050c; non-reactive, control experiment — see Fig. 4(a)) did not result in re-strengthening, as indicated by the

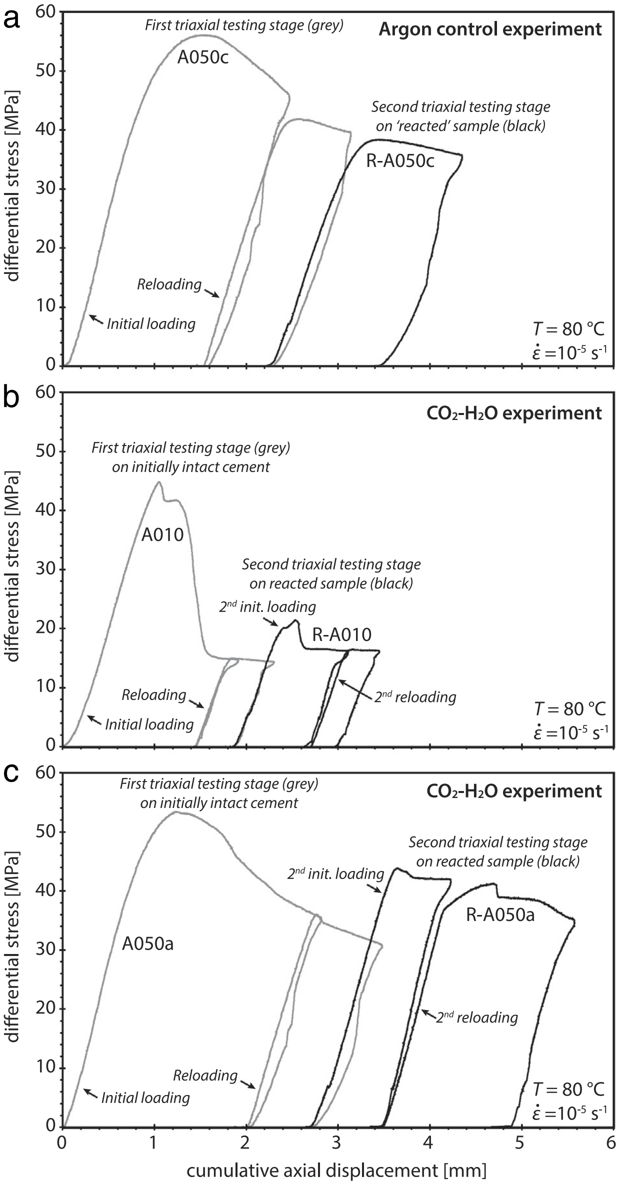

Fig. 4. Differential stress versus cumulative axial displacement data for the fractured and reacted samples (R-series, fracture reactivation experiments). (a) Experiment R-A050c, a control experiment employing argon pressurised water during the "reaction" stage. (b) Experiment R-A010 and (c) experiment R-A050a, employing CO_2-saturated water during reaction. For each sample, the first triaxial testing phase (prior to reaction) is shown in grey, the second triaxial testing phase (post reaction) in black.

absence of a true peak-stress and close correspondence with the unreacted cement strength data from the first triaxial testing stage (i.e. no change in mechanical properties occurred after versus before hydrothermal treatment). By contrast, both cement samples that were reacted with water and CO_2 (R-A010, R-A050a) showed marked re-strengthening, seen as a distinct peak-strength, followed by minor strain-softening towards (near) strain-neutral behaviour. In experiment R-A010 (Fig. 4(b)), $\sigma_{\max}$ measured ∼48% of the peak strength obtained during the first stage of triaxial testing. In experiment R-A050a (Fig. 4(c)) this was ∼83%. In addition, for both samples, the differential stress supported in the post-failure stage was considerably higher (14% in R-A010; 40% in R-A050a) than that supported in the post-failure stage of the initial triaxial testing phase.

3.2. *Macroscopic failure modes during initial deformation*

Externally and in whole-sample section, the deformed-only samples of immature and mature cement showed broadly similar macroscopic failure modes (Fig. 5). At low P_c^{eff} (1 to 10 MPa), samples failed in a brittle to semi-brittle manner, evidenced by distributed near-axial cracks or else localised, sometimes conjugate shear fractures orientated

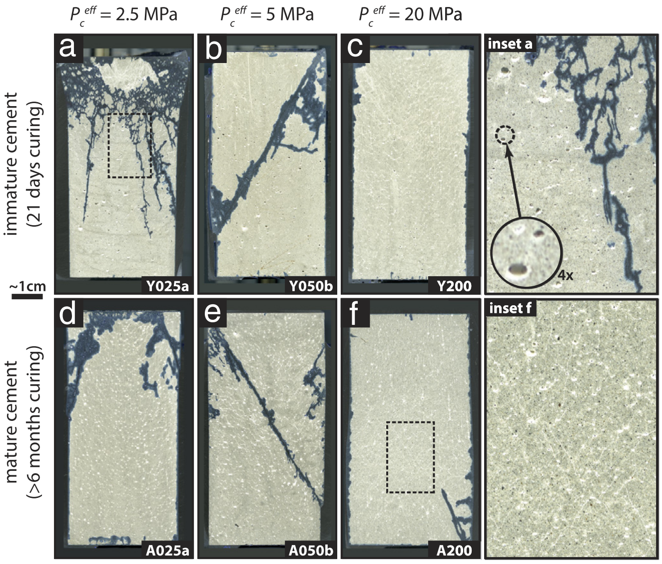

Fig. 5. Photographs of deformed cement samples, where a–c and d–e respectively show the macroscopic failure modes of immature and mature cement with increasing effective confining pressure. Blue colour is due to dyed epoxy used to impregnate the samples. (For interpretation of the references to colour in this figure legend, the reader is referred to the web version of this article.)

at ∼30 ° with respect to σ_1. In specimens that were not impregnated with epoxy, these shear fractures retained cohesion. They typically contain only minor amounts of “fault gouge”, surrounded by a 0.5 to 2 mm wide, microfractured damage-zone (for the major fractures, the extent of the blue-dyed epoxy approximately corresponds to these zones — Fig. 5). At these low confining pressures, flattened macropores were observed in both immature and mature cement, indicating that some ductile deformation of the matrix occurred.

With increasing P_c^{eff} (5 to 25 MPa), macroscopically homogeneous ductile behaviour became more evident in both sample types, with numerous pores showing directly observable flattening (see inset Fig. 5(a)), and an overall reduction in visible porosity, compared to undeformed samples. No localised compaction bands were observed. At these higher confining pressures, only the two samples deformed to high axial strain (>8%) exhibited distributed networks of microcracks, sometimes forming conjugate sets and even shear-fractures, orientated at 25–35° with respect to the compression direction. These samples (A100, A200) display features such as irregular fractures and braided damage zones (1–2 mm), but no loss of cohesion (Fig. 5(f), inset). In the other samples, deformed to lower axial strains, we found no evidence for microcracking.

3.3. Failure mode and chemical alteration of the reacted samples

The fractured samples of mature cement that were subjected to chemical reaction and then re-tested (at the original deformation conditions, i.e. at 80 °C and $P_c^{eff} = 1$ to 5 MPa) deformed in a brittle to semi-brittle manner (Fig. 6(a)–(b)), mainly by reactivation and propagation of pre-existing fractures introduced during the initial triaxial testing phase. Reactivation is demonstrated by the chemically zoned and discoloured nature of the cement surrounding and disrupted by the latest fractures, indicating that these fractures were already present during batch reaction.

The chemical zonation, present in all reacted samples, was prominently visible as an orange-brownish colouration (Fig. 6(a)–(b)), penetrating the outer surface of the samples in addition to bounding larger (pre-existing) fractures. The reaction fronts observed at the outer cylindrical surface of the samples have a combined radial penetration depth of about 2 to 6 mm, while along the fractures they are seen as discontinuous orange zones developed in the fracture plane walls and varying from indiscernibly thin to about 3 mm in width. XRD analysis of samples of orange zone material yielded aragonite (∼58.8 wt%), calcite (∼22.5 wt%), vaterite (∼10.0 wt%) and brownmillerite (∼8.7 wt%), the last being an occasionally surviving cement phase[10,14,18,28]. Though somewhat obscured by the blue-dyed resin used to impregnate and highlight the fracture pattern, a thin (∼50 μm), white layer could be observed at the outermost surface of the reacted cement samples. XRD analysis revealed that this white layer consisted mainly of aragonite (∼80%), calcite (∼20%) and minor vaterite (<5%). Similar material was also locally discernible within the fractures, forming deposits on the fracture surfaces of up to ∼200 μm thick. Optical microscopy revealed that several of the narrower fractures are completely filled with this material, forming crystalline vein-like structures (Fig. 6(c)). Larger fractures often remained partially open, with white acicular aragonite lining the fracture walls (Fig. 6(d)). By contrast, precipitation of calcium carbonates was only sparsely observed in the cement macropores (i.e. air bubbles), though cracks connecting these pores did show some signs of discolouration (Fig. 6(e)).

Fig. 7 shows μXRF single-element distribution maps for Ca, S, Si, Al and Fe, for an area around one of the larger

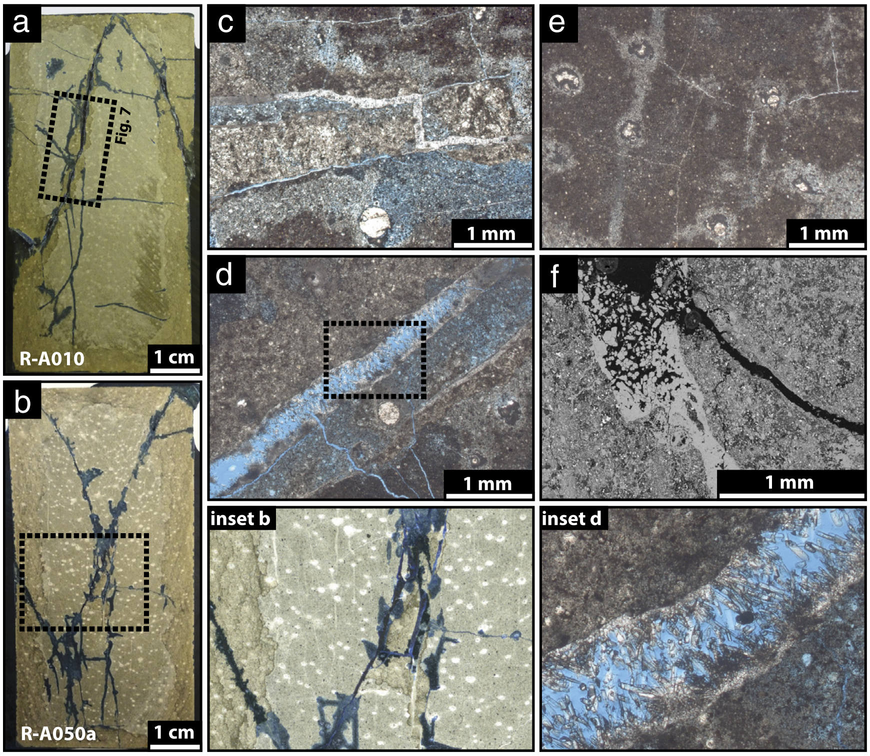

Fig. 6. Photographs of deformed–reacted–deformed samples of mature cement, with the macroscopic failure mode and sample scale reaction-induced zonation for (a) sample R-A010, and (b) sample R-A050b. Furthermore, optical micrographs of sample R-A010, with (c) near-complete calcium carbonate cementation inside a fracture, (d) acicular crystals of aragonite, formed within one of the larger, open fractures, and (e) alteration developed along pathways going from pore to pore. Blue colour in (a–d) is due to dyed epoxy used to impregnate the samples. Finally, (f) SEM micrograph of a newly formed fracture (during second triaxial testing or post-experimental), adjacent to a healed fracture, incurred during initial triaxial testing. (For interpretation of the references to colour in this figure legend, the reader is referred to the web version of this article.)

fractures in sample R-A010 (mapped region indicated in Fig. 6(a)). In these images, the greyscale (defined per element) represents element abundance, with lighter shades corresponding to higher concentrations. Combined, the element maps corroborate the chemically zoned nature of the cement around the fractures. Progressing from the fracture core outward, we first observed the acicular aragonite precipitates lining the fracture walls, here identified by very high Ca concentrations. Within the fracture walls, we found (I) a zone, up to ∼2mm wide, characterised by increased Ca and Si, and decreased Al and S concentrations, followed by (II) a very narrow zone of high Ca concentrations, and (III) a zone of decreased Ca and increased Al and Si concentrations, up to ∼1mm in extent — see the interpretation map (Fig. 7, i). The remainder of the cement appeared relatively unaffected. Comparison of the light and SEM microscopy results showed zone I to be a dense region coinciding with the orange-brownish colouration seen optically, while zone III was greyish optically and relatively porous.

4. Discussion

The current experiments on both mature and immature samples of API-ISO Class G HSR Portland cement, deformed in compression, wet at 80 °C, have shown a transition from semi-brittle failure behaviour at low effective confining pressure (1 to 10 MPa) to more ductile deformation, dominated by strain hardening, at effective confining pressures ranging from 15 to 25 MPa. Our data further demonstrated a modest increase in peak strength with increasing confining pressure, i.e. where a peak was seen (Figs. 2, 3; Table 1). Conversely, yield strength (σ_y) decreased with increasing confining pressure (Table 1). The experiments on fractured, mature cement samples reacted with CO_2 and water under hydrostatic conditions showed fracture reactivation characterised by partial recovery of initial failure strength (up to 83% after six weeks) and an increase in post-failure sliding strength after reaction (up to 40%). In the following, we first discuss alternative methods for the quantification of the yield strength of porous materials, to complement the simple approach used in presenting our results so far. We then use our cement strength data as a basis for deriving both yield and failure criteria for unreacted cement, suitable for use in geomechanical analyses of the wellbore system. We go on to compare our results with previous strength data for wellbore cement. Finally, we discuss the effects of CO_2-induced reactions on strength recovery (i.e. healing) as well as the implications of our findings for well integrity in the context of geological storage of CO_2.

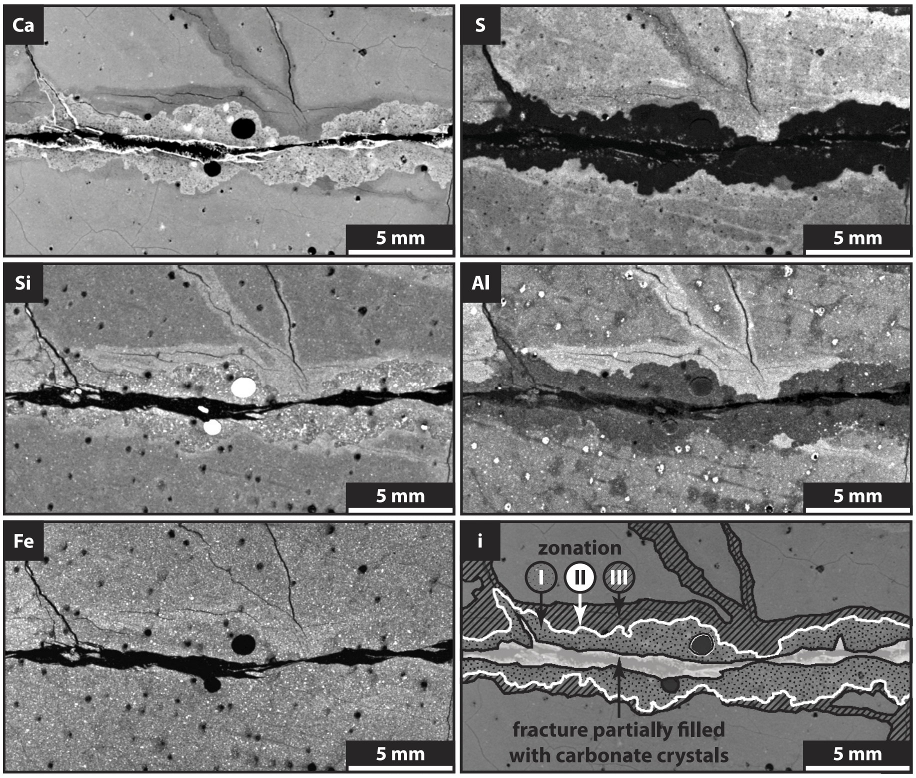

Fig. 7. Micro-X-ray fluorescence maps for Ca, Si, Al, S and Fe, showing an area around one of the larger fractures in sample R-A010 (mapped region is indicated in Fig. 6(a)). Greyscale (defined per element) qualitatively shows element abundance, with bright illumination corresponding to higher concentrations. Alteration zones I to III are schematically indicated on the interpretation map (i).

4.1. Quantification of the onset of inelastic yield in unreacted samples

4.1.1. Mature cement samples

In addition to the method used here to define σ_y[45], the initial yield stress of porous rock materials is often defined in terms of the onset of shear-enhanced compaction, identified by comparing hydrostatic and non-hydrostatic loading data in a plot of effective mean stress (P) versus pore volume change ($\Delta V_{p\%}$)[46]. We adopt this approach in Fig. 8, which shows representative data for our triaxial tests on unreacted mature cement samples (A010, A025a, A050a, A100, A150, A200 and A250), together with reference data obtained from our two hydrostatic compaction experiments (A-HS1 and A-HS2). Note that the approach cannot be applied to our immature samples as no hydrostatic tests were done on these.

Let us first focus on the hydrostatic loading curve of experiment A-HS1 (solid black curve, Fig. 8). This sample was loaded at a rate of roughly 30 MPa h^{-1}, chosen to be comparable with the loading rate achieved in the triaxial experiments, in terms of effective mean stress versus time. Despite minor initial stiffening of the sample (probably related to closure of microcrack porosity), this curve shows an undulating but relatively linear, presumably poroelastic portion up to the point denoted P^*_{A-HS1}, beyond which the curve becomes markedly nonlinear (Fig. 8). This point represents the critical effective pressure, P^* (33.2 MPa, for hydrostatic loading of mature cement at a rate of ∼30 MPa h^{-1}), associated with the onset of inelastic compaction due to hydrostatic pore collapse (following Wong and Baud[46], and references therein).

Turning now to our triaxial data in Fig. 8, deviations from the hydrostatic curve imply that deformation depends on the deviatoric stress and is no longer poroelastic[46,47]. For experiment A010 ($P_c^{eff} = 1$ MPa), the data initially follow the hydrostatic curve. However, at an effective mean stress of about 12.4 MPa, deviation from the hydrostatic curve occurs at C^*, indicating the onset of shear-enhanced compaction. This is followed by a sharp transition from compactant to dilatant behaviour at $C^{*\prime}$ (following the nomenclature of Wong and Baud[46]).

For experiments A025a to A250 ($P_c^{eff} = 2.5$ to 25 MPa; see Table 1), the origins of the triaxial data (i.e. at $P = 2.5$ to 25 MPa) were shifted horizontally in Fig. 8 to lie on hydrostatic curve A-HS1. This is equivalent to assuming that only poroelastic deformation had occurred during application of the effective confining pressure prior to triaxial testing[46]. Treated in this way, the initial parts of the curves obtained in our triaxial tests on mature cement show less net compaction at fixed effective mean stress than hydrostatic curve A-HS1. Recalling our microstructural observations for these samples, it is unlikely that this is related to initial microcracking of the samples compared to the hydrostatic case. More likely, the initial steepening of the triaxial curves, relative to the hydrostatic curve, is caused by stress- and/or time-dependent compaction of the cement samples during

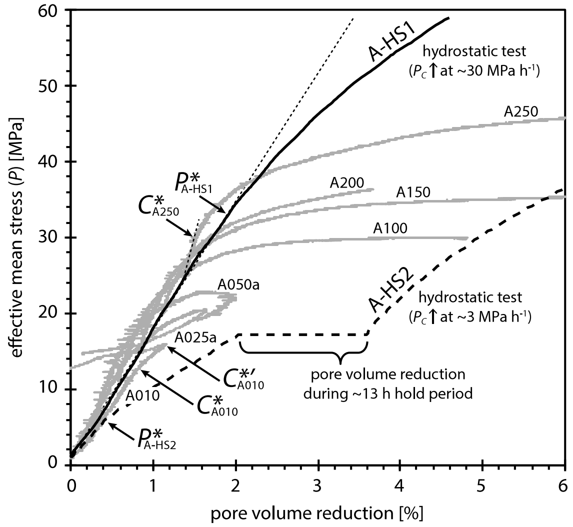

Fig. 8. Effective mean stress (P) versus pore volume change data for representative triaxial compression tests performed on wet, mature cement (A010, A025a, A050a, A100, A150, A200, A250). For comparison, data obtained from two hydrostatic compaction experiments (A-HS1, A-HS2) are also provided. Points denoted P^* are the hydrostatic critical effective pressures, while points denoted C^* and $C^{*\prime}$ are critical stress states for shear-enhanced compaction and dilatation, respectively (nomenclature of Wong and Baud[46]).

pre-test pressurisation and equilibration. Here it should be noted that the initial conditions, i.e. prior to axial loading, for the hydrostatic experiments and for triaxial test A010 were equivalent, while the other triaxially tested samples experienced a higher effective confining pressure during heating and machine equilibration. To approximate the onset of shear enhanced compaction (C^*) for samples A025a to A250, we therefore determined the point at which the effective mean stress versus pore-volumetric strain data deviates from linearity (see example for C^*_{A250} in Fig. 8), using the method previously applied to determine the yield strength from differential stress versus axial strain data[45]. The values for C^* thus obtained are given in Table 1.

In view of the above, the potential impact of loading rate, i.e. of time-dependent compaction, was assessed by comparing the results of experiment A-HS1 with a second hydrostatic compaction experiment (A-HS2), performed at a ten times slower hydrostatic loading rate ($\sim$3 MPa h^{-1}). As seen in Fig. 8 (dashed black curve), the effective mean stress versus pore volume reduction data of the two hydrostatic experiments roughly align up to $P \approx$ 6 MPa. This corresponds to the critical effective pressure (P^*_{A-HS2}) for the more slowly loaded sample (A-HS2), beyond which non-linear behaviour and markedly more compaction occurs. Midway during experiment A-HS2, hydrostatic loading was paused, holding P at 17 MPa for a period of about 13 h, during which significant ($\sim$1.5%) pore volume reduction occurred (Fig. 8). After reinitiation of active hydrostatic loading, the sample showed a steeper curve compared with before the hold period, reflecting increased resistance to compaction after the hold. Together with the similar steepening seen in the early stages of the triaxial curves (compared to the A-HS1 data — see Fig. 8), the results for sample A-HS2 prove that our yield data include some time-dependence, i.e. creep effects.

4.1.2. Immature cement samples

Since no hydrostatic compaction experiments were performed on immature cement, the yield strength of these samples cannot be treated using the method of Wong and Baud[46] described above. However, C^* can be estimated in the same way as for the majority of our mature cement samples, i.e. from the departure from linearity in an effective mean stress (P) versus pore volume change plot (cf. Fig. 8). Applying this procedure to our triaxial tests on immature cement samples led to the C^* estimates given in Table 1. Note they are generally comparable with the values obtained for the mature cement samples.

4.2. Yield and failure criteria for unreacted cement

To delineate baseline yield and failure criteria (i.e. stable versus unstable stress states) for unaltered Class G Portland cement, we now plot our compressive strength data ($\sigma_y, \sigma_{\max}, \sigma_{1\%}, \sigma_{2\%,} P^*$ and C^*) in so-called P–Q space for the first phase of triaxial testing of all immature and mature cement samples — see Fig. 9. P–Q space is widely used to represent the yield and failure behaviour of granular and porous rock materials — see e.g. Roscoe et al.[48], Rutter and Glover[49] and Wong and Baud[46]. Following these authors, P and Q are related to the first and second invariants of the Cauchy stress tensor (I_1) and the deviatoric stress tensor (J_2), respectively, via the relations

$$P = \frac{I_1}{3} - P_f \quad \text{and} \quad Q = \sqrt{3J_2} \tag{1}$$

where

$$\begin{gathered} I_1 = \sigma_1 + \sigma_2 + \sigma_3 \quad \text{and} \\ J_2 = \frac{1}{6}\left[(\sigma_1 - \sigma_2)^2 + (\sigma_2 - \sigma_3)^2 + (\sigma_3 - \sigma_1)^2\right]. \end{gathered} \tag{2}$$

Note that P is the effective mean stress already defined, while Q is a measure of the (octahedral) shear stress. In a hydrostatic loading experiment, $P = P_c^{eff}$ and $Q = 0$. In the case where $\sigma_2 = \sigma_3 = P_c$, as in our conventional triaxial experiments, $P = (\sigma_1 + 2P_c)/3 - P_f$ and Q reduces to the differential stress ($\sigma_1 - P_c$), so that $Q = 3(P - P_c^{eff})$. For uniaxial conditions, $P_c^{eff} = 0$. Stress paths (SP) corresponding to hypothetical uniaxial compressive (UC) and uniaxial tensile (UT) loading are accordingly represented by the lines $Q = \pm 3P$, as plotted in Fig. 9 (dashed grey lines denoted UCSP and UTSP, respectively) for reference purposes.

4.2.1. Brittle failure criteria

We first discuss brittle failure, as this behaviour is expected to have the most profound impact on well integrity. To obtain expressions describing brittle shear failure of cement from our peak-strength ($\sigma_{\max}$) data, we assume a linear or Drucker–Prager criterion[52], written in the form:

$$Q = aP + b \tag{3}$$

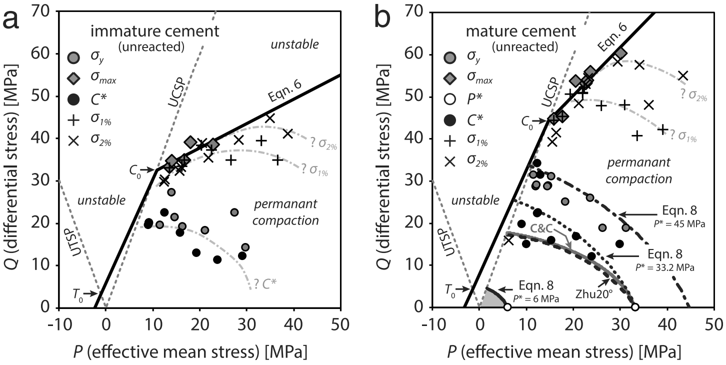

Fig. 9. *P–Q* diagrams showing yield and failure data in terms of $\sigma_{\max}$, C^*, P^*, σ_y, $\sigma_{1\%}$ and $\sigma_{2\%}$ for (a) immature and (b) mature cement. The lines marked UCSP and UTSP denote stress paths for hypothetical uniaxial compressive and uniaxial tensile loading, respectively, added for reference purposes, while T_0 and C_0 denote the unconfined tensile and compressive strengths of the cement. In Fig. 9(b), the solid grey line denoted C&C is a fit to the C^* data employing the shear-enhanced pore collapse model by Curran and Carroll[50]. Similarly, the dashed black line denoted Zhu 20° is a fit to the C^* data employing the Zhu et al.[51] model, assuming a Drucker–Prager criterion with 20° internal friction angle. The three curves denoted Eq. (8) represent end-cap model fits obtained with this equation (see Zhu et al.[51]), using P^* values as indicated. For the immature cement, no model fits to the C^* data were produced (Fig. 9(a)), as P^* was not determined for this material.

where a and b are experimentally determined constants. For our experimental conditions, a and b can be related to the Mohr–Coulomb failure parameters via[53]:

$$a = \frac{6\sin\varphi}{3-\sin\varphi} \quad \text{and} \quad b = \frac{6c\cos\varphi}{3-\sin\varphi}. \tag{4}$$

Further, it is easily shown that

$$C_0 = \frac{2c\cos\varphi}{1-\sin\varphi} = \frac{3b}{3-a}. \tag{5}$$

Here, c denotes cohesion, $\mu = \tan\varphi$ is the coefficient of internal friction, φ is the angle of internal friction and C_0 is the unconfined compressive strength.

Brittle failure of our immature and mature cement samples was in both cases characterised by a peak-strength ($\sigma_{\max}$), which increased with confining pressure (Figs. 2 and 3). The associated macroscopic failure mode indicates that failure occurred mainly via the development of localised shear fractures (Fig. 5). With reference to the *P–Q* plots for the immature and mature samples presented in Fig. 9, the peak-strength data can be fitted reasonably well by linear relationships, given

$$\begin{aligned} Q_{immature} &= 0.58P + 26.3 \\ Q_{mature} &= 1.14P + 27.4. \end{aligned} \tag{6}$$

In terms of the Mohr–Coulomb failure parameters, this yields $C_0 = 32.6$ MPa and $\varphi = 15.1°$ for immature cement. For mature cement, C_0 and φ values of 44.2 MPa and 28.4° are obtained.

From Fig. 9, it is clear that the above Drucker–Prager criteria intersect the uniaxial compressive stress path (UCSP) at the point $Q = C_0$, as expected. Extrapolation of the Drucker–Prager criterion beyond this point to lower P and Q values has no physical meaning, as this would imply stress states involving a negative effective confining pressure and hence extensional rather than shear failure. The brittle failure envelopes were therefore extended to lower P and Q values, to describe extensional failure, as follows. First we estimated the uniaxial tensile strength (T_0), which for cements is typically about one tenth of the uniaxial compressive strength C_0[9,54]. Assuming a linear relationship between T_0 and C_0, given simply as $T_0 = C_0/10$, and using Eqs. (4) and (5), resulted in $Q = (27P + 2C_0)/11$ (following Pariseau[55]). The failure envelopes thus obtained are indicated in Fig. 9 using black, solid lines.

4.2.2. *Criteria for inelastic yield*

Criteria for first yield were obtained by plotting the critical stresses for shear-enhanced compaction (C^*) of our unreacted immature and mature cement samples in *P–Q* space, as shown in Fig. 9(a) and (b), respectively, along with the P^* data for hydrostatically compacted mature samples (Fig. 9(b)). For both sample types, yield strength (σ_y) data are also plotted for comparison (Fig. 9(a)–(b)), but have not been used in the construction of the yield envelopes discussed below.

For both immature and mature cement, the C^* data, as well as the σ_y data, show a negative dependence of Q on P, consistent with a shear-enhanced compaction failure envelope, or end-cap, of the type often obtained from triaxial experiments on porous rock materials[46]. As previously observed by Wong et al.[47] for sandstone, and Zhu et al.[51,56] for limestone and tuff, the C^* data can generally be described using an elliptical fit in *P–Q* space, of the form

$$\frac{(P/P^* - \gamma)^2}{(1-\gamma)^2} + \frac{(Q/P^*)^2}{\delta^2} = 1 \tag{7}$$

where γ and δ are empirical constants, and P^* is the critical hydrostatic pressure for compactant yield[47]. Most of our mature cement C^* data can be described reasonably well using this relation (not shown in Fig. 9), taking $P^* = 33.2$ MPa, as measured, and using γ and δ values of 0.1–0.3 and 0.5–0.7, respectively, which fall close to the range for limestones and tuffs ($\gamma \leq 0.4$, $\delta \geq 0.7$) given by Wong and Baud[46]. No fit of this type could be obtained for the immature cement, as P^* was not determined for this material. Note, however, that the C^* data (and σ_y data) for immature cement, like those for mature cement, clearly delineate an end-cap-like trend with increasing effective mean stress, suggesting a P^* value in the range 25–40 MPa (Fig. 9(a)). Together with the frequent occurrence of flattened macropores in the deformed samples (Fig. 5), the data on C^* and P^* (as well as σ_y) suggest that both the immature and mature cement samples yielded by "shear-enhanced plastic pore collapse"[50,57].

Aside from empirical end-cap criteria for yield (i.e. Eq. (7)), the models proposed by Curran and Carroll[50] and Zhu et al.[51] can potentially be applied to describe yield of our mature cement samples, as the spherical pore geometry assumed in these models is quite realistic for the macropores (air bubbles) present in undeformed cement[9]. Both models consider a single pore surrounded by a linear elastic material governed by a Drucker–Prager yield criterion (or a von Mises criterion, if the internal friction angle is assumed zero, corresponding to perfectly plastic yield). Curran and Carroll[50] provide an analytical solution for a concentric spherical shell of material with inner radius r ($=$ pore radius) and outer radius R, assuming the macroscopic stresses to act on the outer shell surface. By contrast, Zhu et al.[51] used the analytical solution, provided by Timoshenko and Goodier[58], for a spherical pore of radius r, embedded in an infinite medium under stress. The two models converge as $r/R \longrightarrow 0$. In both models, macroscopic yield initiates when the local stresses at the pore wall exceed those specified by the governing Drucker–Prager criterion, resulting in yield criteria, in terms of macroscopic stress state, that are elliptical in P–Q space. Both require P^* data as input, so can only be applied to our mature cement data.

As noted by Vajdova et al.[59], for a variety of porous rock types, the pore collapse models are usually unable to explain combined hydrostatic (P^*) and non-hydrostatic (C^*) yield data using one set of model parameters. Moreover, there is considerable scatter in our data, preventing rigorous comparison and implementation of the models. Therefore, following the approach of Vajdova et al.[59], our mature cement C^* data were bracketed using lower and upper bound model fits (Fig. 9(b)). For all our fitting calculations, we assumed a Poisson's ratio (ν) of 0.25, which is typical for cement[60], noting that deviations have only a small effect on the yield criterion[51]. In applying the Curran and Carroll[50] model to our P–Q data for C^*, we used the equations provided by Baud et al.[57, Appendix]. Following these authors, we selected the ratio r/R such that $(r/R)^3$ equals the measured initial porosity (40.1% ±1.2%), which is equivalent to assuming that R is related to the mean pore spacing. Applied in this way, the Curran and Carrol[50] model, when adjusted to match at $P^*{}_{A-HS1}$, provided a reasonable lower bound envelope to our C^* data, underestimating strength slightly (solid grey line denoted C&C, Fig. 9(b)).

A nearly identical fit to our C^* data for mature cement could be obtained using the Zhu et al.[51] model, employing a Drucker–Prager criterion with an internal friction angle of 20° to describe the matrix material (dashed black line denoted Zhu 20°, Fig. 9(b)). Using a von Mises criterion in the Zhu et al.[51] model instead, provided a somewhat better overall agreement with the complete set of C^* data, especially those obtained in experiments A010 and A025a (dotted black line, Fig. 9(b), cf. Table 1). For this model case, the yield cap takes a simplified form[46,51]:

$$\frac{Q}{P^*} = \frac{3}{20}\frac{7-5\nu}{7\nu^2-13\nu+7} \times \left[\sqrt{4\left(7\nu^2-13\nu+7\right)-27\left(1-\nu\right)^2\left(\frac{P}{P^*}\right)^2} - (1+\nu)\frac{P}{P^*}\right]. \tag{8}$$

The above expression was also used to construct an upper bound envelope for yield of the mature cement. To this end, P^* was adjusted to acquire a best fit to the C^* data obtained in experiments A010 and A025a, i.e. at low effective confining pressure (dashed–dotted black line, Fig. 9(b)). This required P^* to be increased to ∼45 MPa, thereby overestimating the measured P^*_{A-HS1} of 33.2 MPa by ∼36%. Note that this upper bound also brackets our yield strength (σ_y) data reasonably well. The Curran and Carrol[50] model gave a poor upper bound fit to the C^* data, not shown in Fig. 9(b).

The considerable scatter in our data on the yield strength (σ_y, P^*, C^*) of mature samples, does not warrant detailed comparison between the various model fits. However, in more qualitative terms, together with the unconfined compressive loading or stress path (UCSP), all of the yield criteria discussed above for mature cement form a subtriangular region in P–Q space (Fig. 9(b)). Assuming wellbore cement has negligible tensile yield strength, this region represents the stress states where deformation is predominantly poroelastic, for the strain rates imposed on our cement samples during triaxial testing.

4.2.3. *Evolution of the yield envelope with increasing strain*

Focusing now on the stress supported by our samples beyond yield, i.e. at 1% and 2% axial strain, and in the approach to failure at $\sigma_{\max}$, our results for both immature and mature cement show a general tendency for the compactional yield cap to expand with accumulating axial strain (see Fig. 9(a)–(b)). The expansion of the compactional yield cap represents the strain hardening observed in both sample types (Figs. 2 and 3) and is qualitatively similar to the evolution of the yield cap seen in porous sandstones as volumetric strain increases and porosity decreases[61]. It implies inelastic material strengthening or strain hardening until the failure criterion is attained. In this way, at low effective confining pressure ($P_c^{eff} < 10$ MPa), compaction evolves towards shear-induced dilatation (Figs. 2, 3 and 8, A010, point C^*' for mature cement), followed finally by brittle failure via localised shear fracture at the peak-strength (∼1% axial strain). Conversely, at higher effective confining pressure ($P_c^{eff} > 10$ MPa), shear-enhanced compaction dominates deformation — see Figs. 2, 3 and 8.

4.2.4. Effect of time-dependence on the yield strength criteria

The inability of the end-cap models[51,50] to unify our experimental yield data for mature cement may be related to several possible reasons. For example, while the macropores in cement paste are near-spherical, the model pore-geometry is idealised and simplified, and does not account for the nano-porous nature of the cement matrix (i.e. the gel-porosity). Also, potential effects of chemical processes such as dissolution[62] are not accounted for in the models considered. Moreover, it is likely that our measured yield strength data contain significant components of time-dependent (i.e. inelastic) deformation or creep. This possibility is most apparent in our mean effective stress versus relative pore volume change data (Fig. 8), where hydrostatic experiment A-HS1 showed more compaction than any of the triaxial experiments conducted at $P_c^{eff} > 1$ (Table 1; see Section 4.1). As the strain rates and loading rates employed in the hydrostatic and triaxial compression tests are inevitably different, time-dependent processes, and different degrees of strain-hardening, may result in different strength envelopes, producing scatter in the data. This further implies that the poroelastic region in P–Q space may be smaller than indicated by our yield data, especially if lower strain rates are considered. To demonstrate this rate-sensitivity of the yield strength criteria, we used Eq. (8) to obtain a yield cap model fit to the critical effective pressure of $P^* \approx 6$ MPa obtained in hydrostatic experiment (A-HS2), which was pressurised ten times slower. As shown in Fig. 9(b) (see greyed area), this entails a substantial decrease in the size of the yield cap, compared with the one roughly delineated by our triaxial data. As such, caution is needed in applying such yield cap envelopes to low deformation rates in geomechanical models.

4.2.5. Comparison with previous data on cement yield and failure

In Fig. 10, the above yield and failure data for unreacted immature and mature cement are compared with yield (σ_y) and failure ($\sigma_{\max}$) data previously obtained for Class G Portland cement. The available previous data are on samples cured for 28 days by immersion in lime solution and tested at room temperature[38] and 90 °C[29,37]. Our immature samples (21 days curing) failed at slightly lower, but comparable peak differential stresses ($\sigma_{\max}$), while the peak-strengths supported by our mature cement samples (>6 months curing) plot about 10%–20% higher than previously reported for 28-day samples. This may be explained by the strengthening that is generally observed with ongoing hydration, associated cement densification and homogenisation[63,64]. Overall, there is reasonable agreement between our data and those of Xie et al.[38] regarding the yield strength (σ_y), though our data show significantly (~30%) lower yield strength at higher effective confining pressures ($P_c^{eff} = 10$–25 MPa). This could be related to the aforementioned rate-effects. Alternatively, it may be due to curing conditions, as we used water instead of lime solution for long-term curing. Although the fluid-to-cement ratio was low during curing of our samples, this may have resulted in portlandite dissolution, potentially generating minor additional porosity. On the other hand, under down-hole conditions, similar dissolution processes can be expected to play a role due to reaction between the alkaline cement and less alkaline formation fluids[65], so that our data may be more realistic.

4.3. Effect of CO_2-induced reactions on the composition and mechanical properties of cement

We now consider the effects of the chemical reaction stage of our experiments, recalling that, following the first phase of triaxial testing of mature samples, selected shear-fractured examples were reacted with CO_2 plus H_2O under hydrostatic conditions ($T = 80$ °C, $P_f = \sim 12$ MPa, $t = 6$ w) and then re-deformed (R-series, Table 1). Compared with the single control experiment (R-A050c) performed using Ar plus H_2O, reaction with CO_2-saturated water resulted in re-strengthening of the samples via the reappearance of a peak-strength ($\sigma_{\max}$ data are plotted in Fig. 10), as well as in increased post-failure frictional strength (Fig. 4). From our microstructural and mineralogical observations, we infer that this re-strengthening is related to calcium carbonate precipitation (Figs. 6 and 7), leading to cementation of the fractures. In the following, we compare our findings with previous studies of the effects of CO_2-induced reactions on the mechanical properties of cement, in an attempt to explain our experimental observations in more detail.

4.3.1. Effect of reaction on unfractured cement: previous work

We begin by considering previous work on reactions in mechanically intact (i.e. unfractured) cement, treating this as a chemical reference system. It is well-established that exposure of unfractured Portland-based cement to a CO_2-bearing aqueous fluid leads to pH-buffering of the cement pore fluid by dissolution of portlandite ($Ca(OH)_2$) and de-calcification of the calcium silicate hydrate (C-S-H) phases, plus precipitation of calcium carbonates and alumino-silicates[4,10,11,18,28,66,67]. Within the cement matrix, these fluid–cement interactions are generally diffusion-controlled[16,68] and hence typically produce a series of alteration fronts[69,70]. From the exposed surface of the cement to its interior, the following reaction zones have been widely identified: (Z1) an extensively-leached, amorphous alumino-silicate dominated zone, (Z2) a zone characterised by calcium carbonate precipitates, (Z3) a portlandite-depleted cement zone and (Z4) unaltered cement[4,10,11,28,67]. Note that zones (I + II) and III, observed in our experiments, correspond well with Z2 and Z3, respectively. These chemical reactions involve changes in composition, specific surface area and porosity that may affect the mechanical properties of the cement.

Occurrence of the above reactions in mechanically intact cement results in a transition from a more-or-less homogeneous material to a mechanically heterogeneous material, complicating bulk mechanical characterisation[63,71]. For this reason, most mechanical data available in the literature are derived from scratch hardness and micro- or nano-indentation measurements, made on individual reaction zones. These show Young's modulus progressively decreases with reaction, by respectively ~25%,

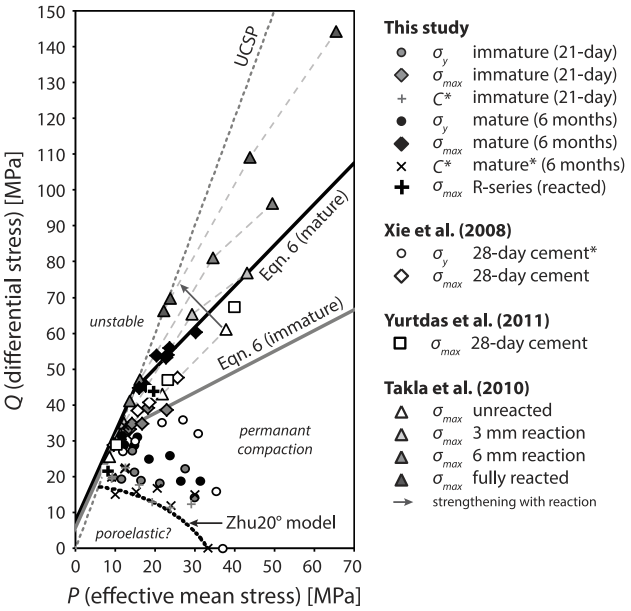

Fig. 10. P–Q diagram comparing the results of the present study with previous literature data. *Including appropriate P^* data. The dotted grey line marked UCSP denotes the stress path for hypothetical uniaxial compressive loading, added for reference purposes. The dark grey arrow and dashed light grey lines are added to illustrate cement strengthening as observed by Takla et al.[29]. Note that the data reported by Takla et al.[29] involved reaction with wet subcritical CO_2, opposed to reaction with CO_2-saturated water employed in the present study.

∼36% and ∼66% for zones Z3, Z2 and Z1, compared to unaltered cement (Z4)[28,71–73]. Hardness measurements[28,67,72] indicate weakening (5%–90%) in the portlandite-depleted cement zone (Z3), strengthening (10%–210%) at locations of calcium carbonate precipitation (Z2), and variable change (from 40% weakening to 25% strengthening) in the amorphous zone (Z1). Note that all of these measurements were performed on dried samples, so likely overestimate the strength of wet material[28,74].

Though the cylindrical samples used were likely non-uniformly reacted, mechanical tests by Chang and Chen[63] on concrete reacted with CO_2 for one year under ambient conditions (23 °C, 20%-CO_2 atmosphere, 70% RH) have shown that while porosity decreased 16%, compressive strength and Young's modulus increased 55% and 17%, respectively. Similar findings have been reported for Class A and Class G Portland cements exposed to CO_2 under conditions more representative for geological storage[25,26]. This reaction-induced strengthening is illustrated in Fig. 10 using peak-strength data obtained by Takla et al.[29] from uniaxial and triaxial compression experiments performed on mechanically intact, cement samples reacted with wet, subcritical CO_2 at 90 °C.

4.3.2. *Effect of reaction on fractured cement: present findings*

4.3.2.1. Chemical zonation. In previous experiments on cement containing (simulated) fractures, employing both (near-)static[13,75] and through-flowing pore fluid[18,21,22,24], reaction zones Z1 to Z3 (see Section 4.3.1) tended to develop subparallel to the fracture surfaces. In our deformed samples subjected to six weeks of reaction with CO_2 (see aforementioned zones in Fig. 7) zones Z2 (cf. I + II) and Z3 (cf. III) can be clearly recognised around the fractures present, while zone Z1 is presumably indiscernibly thin or more likely obscured by the deformation that occurred during the second triaxial phase. Compared to typical literature values, relatively thick alteration rims (mainly Z2) formed in our samples, reaching up to 6 mm at the outside of the samples. This could be related to curing conditions[76], but may also be related to the presence of microcracks, created during initial triaxial testing. The alteration zones bounding the fractures present in our samples are thinner than those at the outside surface, probably reflecting the availability of reactive material (in the fractures cement is present on both sides). Reaction at the sample surfaces may also have been aided by a relatively easy access of fluid, compared to the fracture surfaces, due to the FEP sleeve not effectively sealing against the cement sample surface under the unconfined conditions used for reaction. Conversely, along-fracture saturation of the reacting fluid may have resulted in the narrower alteration zones and the partial-infilling of fractures by the aragonite precipitates observed (Fig. 6(c)–(d)). Aragonite occurs abundantly in wellbore cement cores obtained from the natural CO_2-bearing reservoir investigated by Crow et al.[15], so may be the true reaction product in the present and similar experiments conducted at 80 °C[42]. However, it has also been associated with rapid pore fluid degassing in fractures[77] and it cannot be excluded that the aragonite precipitates are related to pressure-loss occurring in the vessel during reaction (up to 5 MPa — see Section 2.6) or upon experiment termination.

4.3.2.2. Effects on mechanical behaviour. In fractured cement samples, bulk-scale mechanical behaviour will, to a large extent, be controlled by the properties of the fractures[78]. It is, therefore, reasonable to interpret our triaxial test data on the deformed and reacted samples (R-series, Table 1) in terms of changes in properties of the fracture surfaces. Our fractured cement samples showed partial strength recovery, evidenced by the reappearance of a well-defined peak-strength (up to 83% recovered), along with a general increase (14%–40%) in the post-failure frictional strength (Fig. 4). Given our microstructural and chemical observations, we infer that this strengthening is likely dominated by cementation of the fractures by calcium carbonates, mainly in the form of aragonite (Figs. 6 and 7). Our interpretation is that this cementation leads to the increased peak and frictional strength because (a) carbonates are relatively strong minerals[79] and (b) precipitation can result in a reduced local porosity[80]. Similar cementation was found by Liteanu and Spiers[13], who observed marked homogenisation and a high calcium carbonate coverage (about 80%) of fracture surfaces in Class A Portland cement reacted with CO_2 for 90 days under similar conditions.

A further contribution to the observed increase in the post-failure (frictional) strength of our samples may lie in reaction-enhanced deformability of solid–solid contact points in the chemically depleted reaction zones (see Section 4.3.1) lining the fracture walls[28]. This has previously been invoked as an aperture closure (or "asperity weakening") mechanism by Huerta et al.[19,33] and Walsh et al.[23]. In fractures subject to a normal stress, asperity-weakening of this type can lead to increased contact area across the fracture that translates into increased frictional strength. Such a mechanism would be dependent on confining pressure, which is consistent with the fact that in our experiments a larger increase in post-failure strength was observed at $P_c^{eff} = 5$ MPa than at $P_c^{eff} = 1$ MPa (cf. R-010 and R-050a, Fig. 4). If the fracture surfaces were to consist of relatively strong asperities (e.g. calcium carbonate precipitates) positioned on a relatively weak, deformable substrate (reaction zones Z1 and Z3), this could similarly lead to an increased contact area across the fracture, as asperities indent into the matrix. However, as no asperity-related effects were observed in the microstructure of our reacted samples, and as the re-shearing strength of fractured rock samples generally increases with P_c^{eff}, even without reaction[78], asperity weakening or indentation effects are believed to be of subordinate importance to calcium carbonate cementation. Note that, compared to the observations by Huerta et al.[19,33] and Walsh et al.[23], our static reaction experiments produced relatively little zone Z1 amorphous material, which may have limited the potential for softened asperities.

4.4. Implications for well integrity in CO_2 storage systems

From a geomechanical point of view, loss of sealing-capacity in wells can be related to fracturing of the cement, debonding at the casing–cement-formation interfaces, or both. This type of structural damage can develop in several ways, starting with (inadequate) well completion and abandonment[81]. Inherent to the hydration reactions involved, Portland cement shrinks during setting and hardening[9,82], which results in radial deformation that may be expressed by cracking of the cement sheath[30] and debonding at the casing–cement and/or cement-formation interfaces[30,75,83]. Bearing in mind that most fractures within the cement or at its interfaces will, at least initially, be of limited vertical extent, and considering that transport in such defects is generally governed by diffusion[42,82], the present experiments, involving reaction in the presence of a static fluid phase, can be expected to be relevant to the behaviour of wells that contain fractures and other flaws, but are free of major, through-going leakage pathways.

4.4.1. Inferences from our mechanical data

The yield and failure criteria for our unreacted cement samples (Fig. 9) can be used to provide constraints on stable versus unstable compressive stress states for cement seals in a well system. This in turn will determine the vulnerability to access by reactive CO_2-rich fluids. Our σ_{max} data show that cement, like most rock materials, is most prone to dilatational shear failure, hence permeability enhancement, under conditions of low effective mean stress plus high differential stress. Whether these failure conditions are reached in a well depends on the initial state of stress in the cement seals and the subsequent changes in downhole temperature and stress state, caused during hydrocarbon production and/or CO_2 storage[30–32,84–86]. Unfortunately, it is far from trivial to determine the initial state of stress in cement seals, or how this evolves, with any certainty[87,88]. Nonetheless, our cement failure data imply that it is generally desirable for the cement to remain under high isostatic confinement (i.e. high P relative to Q), to inhibit dilatational modes of failure.

More importantly, our yield data demonstrate that cement easily compacts via permanent, irreversible deformation processes if subjected to increasing isostatic confinement or effective mean stress. This tendency is widely recognised and has been attributed here to pore collapse (see also Jennings[89]), though sliding of C-S-H sheets has also been invoked[90]. Irrecoverable compaction will play a key role in well integrity, as its occurrence implies that reversals in the stress path experienced by the cement seals of a legacy well, such as (a) cyclic loading and unloading during its production-life, or (b) reservoir depletion followed by re-pressurisation during CO_2 storage, can result in stress–strain incompatibilities, which in turn may lead to failure, in particular tensile failure. Reversals in the wellbore stress path, especially if this migrates outside the apparently elastic region defined in P–Q space by the UCSP and Eqs. (7) and (8), should therefore be avoided. In this way, the present experiments demonstrate that it is essential to include the inelastic compaction behaviour of cement and yield plus failure criteria such as ours in geomechanical analyses of the wellbore system, corroborating previous assessments by Bois et al.[91]. It should be noted, however, that the yield (and failure) criteria for cement are sensitive to time and rate-effects, as demonstrated by our second hydrostatic loading experiment (A-HS2), which implies a significant reduction in yield strength for slower deformation-rates (see greyed area, Fig. 9(b)). A more systematic study of the importance of these time and rate-effects is clearly needed.

The above-mentioned uncertainties regarding the initial stress state and its subsequent evolution (both of which will be well-specific), inevitably complicate failure analysis. Nonetheless, even if the cement initially provides an adequate hydraulic seal, it is generally likely that some fractures and/or debonding defects will develop, which may grow and interconnect due to ongoing changes in downhole temperature and stress state[30–32,84–86]. The implications this has for well integrity not only depend on whether failure occurs, but also on the location and along-well extent of the defect[17,91], and on subsequent interaction with any migrating fluid.

4.4.2. Effects of chemical reaction on wellbore integrity

While the possibility of leakage pathway formation due to stress or temperature changes in the wellbore certainly cannot be excluded on basis of the present data, our reaction–reactivation experiments show that CO_2-induced chemical reactions do not lead to chemical–mechanical weakening of fractured cement, at least not under the static conditions outlined above (Fig. 10). Rather, our results suggest more or less complete strength recovery on timescales in excess of those used in our experiments (six weeks). This implies that previously reported self-sealing (i.e. reaction-induced permeability reduction) of fractures in cement exposed to CO_2[12,13,24,92] is unlikely to be negated by fracture reactivation. Instead we observed considerable and fast CO_2-induced healing (up to 83% of peak strength recovered, plus up to 40% increased post-failure frictional strength in six weeks reaction-time — Fig. 4). This suggests that the cement components of a well situated in CO_2-storage environments may actually be less prone to fracture propagation and coalescence, than in CO_2-free environments (cf. experiment R-A050c), if CO_2-induced healing outstrips the rate of damage accumulation. Note, however, that the self-healing capacity of cement undergoing repeated fracture may be affected by depletion of reactive cement phases upon repeated re-exposure to CO_2-bearing fluid.

The alteration along the fractures appears variable and locally discontinuous in the present experiments. While this potentially allows for specific channels to remain open, rapidity of the reactions suggests that, on longer time scales, strength recovery (i.e. healing) will likely be accompanied by ongoing permeability reduction (i.e. sealing), similar to that observed elsewhere[13,24,92]. It should be noted, however, that this does not necessarily mean that an impermeable state will be attained.

4.4.3. Tensile failure

The tensile yield and failure strength of cement have not been rigorously considered in the present experimental investigation. Additional experiments, exploring stress-states including tensile components, are needed for a full evaluation of the chemical–mechanical impact of CO_2-induced reactions on the mechanical integrity of wellbore cement. However, given the low bond strength of cement–casing and cement-formation interfaces, typically only 0.1–3 MPa[54,82,93,94], and given the large jump in mechanical properties at these sites, hence scope for stress–strain incompatibility, especially at the casing–cement interface (casing steel is 25–50 times stiffer than cement and rock[30]), tensile failure can be expected to occur mainly at the material interfaces within the well system. Such interfacial debonding defects could potentially propagate along the well trajectory via a hydraulic fracturing mechanism[82,95,96]. More research is required to assess the effects of CO_2-induced chemical reactions on this type of potential leakage pathways[42,75,97,98].

5. Conclusions

The present experiments have addressed (a) the yield plus failure behaviour of intact cement and (b) whether CO_2-induced reactions, occurring within fractures in pre-fractured cement, can lead to self-enhancing, chemical–mechanical weakening effects that can potentially maintain leakage pathways open dynamically. The experiments consisted of triaxial compression tests on wet API-ISO Class G HSR Portland cement cylinders (two types, namely: immature, 21 days curing, and mature, >6 months curing), conducted under down-hole conditions that could promote fracturing ($T = 80$ °C, $P_c^{eff} = 1$–25 MPa). After deformation, selected fractured samples of mature cement were reacted with CO_2-saturated/pressurised water ($T = 80$ °C, $P_f = \sim 12$ MPa, $t = 6$ weeks), or with Ar-pressurised water (control experiment), and subsequently subjected to a second triaxial compression test, in order to observe any effects of CO_2-induced reactions on the post-failure (fracture) strength. Our findings can be summarised as follows:

1. Under all effective confining pressures investigated ($P_c^{eff} = 1$–25 MPa), both immature and mature cement yields by shear-enhanced compaction. With accumulating strain, at $P_c^{eff} < 10$ MPa, this gives way to dilatant behaviour shortly prior to failure, the latter manifested by localised, semi-brittle shear fractures. At higher P_c^{eff}, yielding is followed by pervasive ductile deformation, invariably marked by strain hardening and continued shear-enhanced compaction.
2. Our failure data show that cement, like most rock materials, is most prone to dilatational forms of failure that can lead to enhanced permeability at low effective mean stress conditions. The shear failure of our cement samples can be described in conventional P–Q space using Drucker–Prager criteria, with $Q = 0.58P + 26.3$ and $Q = 1.14P + 27.4$ (values in MPa) for immature and mature cement, respectively. Our yield data can be reasonably described in P–Q space using empirical elliptical yield cap fits and various pore collapse models, notably that of Zhu et al.[51]. However, evidence was found for time-dependence (strain-rate dependence) of the various envelopes constructed, so that caution is needed in applying these envelopes to low deformation rates. A more systematic study of the importance of these time and rate-effects is needed.
3. Nonetheless, our yield data demonstrate clearly that cement readily compacts irreversibly if subjected to an increase in effective mean stress. Accordingly, reversals in the well stress path (i.e. loading followed by unloading) should be avoided during well operations, because the cement will not be able to accommodate re-expansion upon unloading, leading to stress–strain incompatibilities and potentially to tensile failure. It is therefore essential that this irrecoverable compaction behaviour is

considered and that yield envelopes of the type constructed here are made use of in geomechanical analyses of well integrity.

4. The pre-fractured samples of mature cement that were reacted with CO_2/H_2O under static conditions showed several reaction fronts that formed parallel to fracture and sample surfaces, involving zones of cement depletion and of calcium carbonate precipitation that are typical of CO_2-induced cement alteration. The second stage of mechanical testing of these samples showed a substantial (up to 83%) recovery of peak-strength, together with an increased (up to 40%) post-failure frictional strength of the samples, both of which can be attributed to cementing by calcium carbonates as a consequence of six weeks of reaction with CO_2–H_2O.
5. Previous work has shown that CO_2-induced reactions can improve the sealing properties of fractured cement (i.e. sealing). Our results demonstrate that this self-sealing effect is not compromised by chemical–mechanical interactions, under conditions where there are no continuous leakage pathways allowing for advective removal of mass. Instead, static reaction induces significant healing, inhibiting reactivation and dynamic reopening of the fractures.
6. While cement seals may be susceptible to failure (either within the bulk or at material interfaces) upon changes in down-hole temperature or stress state, e.g. due to well operations, the present findings suggest that the processes leading to failure are not enhanced or accelerated, but counteracted by CO_2-induced reactions, at least under static fluid conditions. As such, a well exposed to CO_2 may actually be more resilient to leakage pathway formation, compared to a CO_2-free well exposed to the same changes in downhole temperature and stress state.

Acknowledgements

We like to thank Eimert de Graaff, Gert Kastelein, Peter van Krieken, Thony van der Gon Netscher, Otto Stiekema, Leonard Bik and Tilly Bouten, for valuable technical support provided in the laboratory, as well as two anonymous reviewers, for their helpful feedback on the first version of the manuscript. This research was conducted within the context of CATO-2 (www.co2-cato.org), the Dutch national research program on Carbon Capture and Storage technology (CCS). The program is financially supported by the Dutch government (Ministry of Economic Affairs) and the CATO-2 consortium parties (NLFES0906).

References

[1] Celia MA, Nordbotten JM, Bachu S, Dobossy M, Court B. Risk of leakage versus depth of injection in geological storage. *Energy Procedia*. 2009;1:2573–2580. http://dx.doi.org/10.1016/j.egypro.2009.02.022.

[2] Gasda SE, Bachu S, Celia MA. Spatial characterization of the location of potentially leaky wells penetrating a deep saline aquifer in a mature sedimentary basin. *Environ. Geol.* 2004;46:707–720. http://dx.doi.org/10.1007/s00254-004-1073-5.

[3] Zhang M, Bachu S. Review of integrity of existing wells in relation to CO_2 geological storage: What do we know? *Int. J. Greenh. Gas Control.* 2011;5:826–840. http://dx.doi.org/10.1016/j.ijggc.2010.11.006.

[4] Barlet-Gouédard V, Rimmele G, Porcherie O, Quisel N, Desroches J. A solution against well cement degradation under CO_2 geological storage environment. *Int. J. Greenh. Gas Control.* 2009;3:206–216. http://dx.doi.org/10.1016/j.ijggc.2008.07.005.

[5] Brandl A, Cutler J, Seholm A, Sansil M, Braun G. Cementing solutions for corrosive well environments. *SPE Drill. Complet.* 2011; 26:208–219. http://dx.doi.org/10.2118/132228-PA.

[6] Hofstee C, Seeberger F, Orlic B, Mulders F, Van Bergen F, Bisschop R. The feasibility of effective and safe carbon dioxide storage in the De Lier gas field. *First Break.* 2008;26:53–57.

[7] Whittaker S, Rostron B, Hawkes C, Gardner C, White D, Johnson J, et al. A decade of CO_2 injection into depleting oil fields: Monitoring and research activities of the IEA GHG Weyburn–Midale CO_2 monitoring and storage project. *Energy Procedia*. 2011;4:6069–6076. http://dx.doi.org/10.1016/j.egypro.2011.02.612.

[8] Montgomery CT. In: Nelson EB, Guillot D, eds. *Implications of Cementing for Well Production and Performance*. second ed. Schlumberger: Well Cem; 2006:773.

[9] Taylor HFW. *Cement Chemistry*. London, UK: Academic Press Limited; 1992.

[10] Kutchko BG, Strazisar BR, Dzombak DA, Lowry GV, Thaulow N. Degradation of well cement by CO_2 under geologic sequestration conditions. *Environ. Sci. Technol.* 2007;41:4787–4792. http://www.ncbi.nlm.nih.gov/pubmed/17695930.

[11] Kutchko BG, Strazisar BR, Lowry GV, Dzombak DA, Thaulow N. Rate of CO_2 attack on hydrated Class H well cement under geologic sequestration conditions. *Environ. Sci. Technol.* 2008;42:6237–6242. http://www.ncbi.nlm.nih.gov/pubmed/18767693.

[12] Bachu S, Bennion DB. Experimental assessment of brine and/or CO_2 leakage through well cements at reservoir conditions. *Int. J. Greenh. Gas Control.* 2009;3:494–501. http://dx.doi.org/10.1016/j.ijggc.2008.11.002.

[13] Liteanu E, Spiers CJ. Fracture healing and transport properties of wellbore cement in the presence of supercritical CO_2. *Chem. Geol.* 2011;281:195–210. http://dx.doi.org/10.1016/j.chemgeo.2010.12.008.

[14] Carey JW, Wigand M, Chipera SJ, WoldeGabriel G, Pawar R, Lichtner PC, et al. Analysis and performance of oil well cement with 30 years of CO_2 exposure from the SACROC Unit, West Texas, USA. *Int. J. Greenh. Gas Control.* 2007;1:75–85. http://dx.doi.org/10.1016/S1750-5836(06)00004-1.

[15] Crow W, Carey JW, Gasda S, Brian Williams D, Celia MA. Wellbore integrity analysis of a natural CO_2 producer. *Int. J. Greenh. Gas Control.* 2010;4:186–197. http://dx.doi.org/10.1016/j.ijggc.2009.10.010.

[16] Duguid A. An estimate of the time to degrade the cement sheath in a well exposed to carbonated brine. *Energy Procedia*. 2009;1: 3181–3188. http://dx.doi.org/10.1016/j.egypro.2009.02.101.

[17] Carey JW. Geochemistry of wellbore integrity in CO_2 sequestration: Portland cement-steel-brine-CO_2 interactions. *Rev. Mineral. Geochem.* 2013;77:505–539.

[18] Wigand M, Kaszuba JP, Carey JW, Hollis WK. Geochemical effects of CO_2 sequestration on fractured wellbore cement at the cement/caprock interface. *Chem. Geol.* 2009;265:122–133. http://dx.doi.org/10.1016/j.chemgeo.2009.04.008.

[19] Huerta NJ, Bryant SL, Strazisar BR, Kutchko BG, Conrad LC. The influence of confining stress and chemical alteration on conductive pathways within wellbore cement. *Energy Procedia*. 2009;1:3571–3578. http://dx.doi.org/10.1016/j.egypro.2009.02.151.

[20] Yalcinkaya T, Radonjic M, Willson CS, Bachu S. Experimental study on a single cement-fracture using CO_2 rich brine. *Energy Procedia*. 2011;4:5335–5342. http://dx.doi.org/10.1016/j.egypro.2011.02.515.

[21] Abdoulghafour H, Luquot L, Gouze P. Characterization of the mechanisms controlling the permeability changes of fractured cements flowed through by CO_2-rich brine. *Environ. Sci. Technol.* 2013;47:10332–10338. http://dx.doi.org/10.1021/es401317c.

[22] Luquot L, Abdoulghafour H, Gouze P. Hydro-dynamically controlled alteration of fractured Portland cements flowed by CO_2-rich brine. *Int. J. Greenh. Gas Control.* 2013;16:167–179. http://dx.doi.org/10.1016/j.ijggc.2013.04.002.

[23] Walsh SDC, Mason HE, Du Frane WL, Carroll SA. Mechanical and hydraulic coupling in cement–caprock interfaces exposed to carbonated brine. *Int. J. Greenh. Gas Control.* 2014;25:109–120. http://dx.doi.org/10.1016/j.ijggc.2014.04.001.

[24] Cao P, Karpyn ZT, Li L. Self-healing of cement fractures under dynamic flow of CO_2-rich brine. *Water Resour. Res.* 2015; http://dx.doi.org/10.1002/2014WR016162.

[25] Liteanu E, Spiers CJ, Peach CJ. Failure behaviour wellbore cement in the presence of water and supercritical CO_2. *Energy Procedia*. 2009; 1:3553–3560. http://dx.doi.org/10.1016/j.egypro.2009.02.149.

[26] Condor J, Asghari K. Experimental study of stability and integrity of cement in wellbores used for CO_2 storage. *Energy Procedia*. 2009;1: 3633–3640. http://dx.doi.org/10.1016/j.egypro.2009.02.159.

[27] Lee K, Kuo C, HSIEH C, HSIANG H, WANG C. Study of mechanical and microscopic properties of API G cement with additives exposed to CO_2-rich environment. *Rock Soil Mech.* 2011;32:346–350.

[28] Mason HE, Du Frane WL, Walsh SDC, Dai Z, Charnvanichborikarn S, Carroll SA. Chemical and mechanical properties of wellbore cement altered by CO_2-rich brine using a multianalytical approach. *Environ. Sci. Technol.* 2013;47:1745–1752. http://dx.doi.org/10.1021/es3039906.

[29] Takla I, Burlion N, Shao J-F, Saint-Marc J, Garnier A. Effects of the storage of CO 2 on multiaxial mechanical and hydraulic behaviors of oil-well cement. *J. Mater. Civ. Eng.* 2010;23:741–746.

[30] Orlic B. Some geomechanical aspects of geological CO_2 sequestration. *KSCE J. Civ. Eng.* 2009;13:225–232. http://dx.doi.org/10.1007/s12205-009-0225-2.

[31] Mainguy M, Longuemare P, Audibert A, Lécolier E. Analyzing the risk of well plug failure after abandonment. *Oil Gas Sci. Technol. Rev.* 2007;62:311–324. http://dx.doi.org/10.2516/ogst.

[32] Lewis K, Zyvoloski GA, Kelkar S, Carey JW. Coupled stress and flow along interfaces in the wellbore environment in relation to CO_2 sequestration. In: *46th US Rock Mech. Symp*. American Rock Mechanics Association; 2012.

[33] Huerta NJ, Hesse MA, Bryant SL, Strazisar BR, Lopano CL. Experimental evidence for self-limiting reactive flow through a fractured cement core: implications for time-dependent wellbore leakage. *Environ. Sci. Technol.* 2013;47:269–275. http://dx.doi.org/10.1021/es3013003.

[34] Nelson EB, Michaux M. In: Nelson EB, Guillot D, eds. *Chemistry and Characterization of Portland Cement*. Schlumberger: Well Cem.; 2006:773.

[35] Nelson EB, Barlet-Gouédard V. In: Nelson EB, Guillot D, eds. *Thermal Cements*. second ed. Schlumberger: Well Cem.; 2006.

[36] Heukamp FH, Ulm F-J, Germaine JT. Poroplastic properties of calcium-leached cement-based materials. *Cem. Concr. Res.* 2003;33: 1155–1173. http://dx.doi.org/10.1016/S0008-8846(03)00024-3.

[37] Yurtdas I, Xie SY, Burlion N, Shao JF, Saint-Marc J, Garnier A. Influence of chemical degradation on mechanical behavior of a petroleum cement paste. *Cem. Concr. Res.* 2011;41:412–421. http://dx.doi.org/10.1016/j.cemconres.2011.01.008.

[38] Xie SY, Shao JF, Burlion N. Experimental study of mechanical behaviour of cement paste under compressive stress and chemical degradation. *Cem. Concr. Res.* 2008;38:1416–1423. http://dx.doi.org/10.1016/j.cemconres.2008.06.011.

[39] Peach CJ. *Influence of Deformation on the Fluid Transport Properties of Salt Rocks*. Utrecht University; 1991.

[40] Peach CJ, Spiers CJ. Influence of crystal plastic deformation on dilatancy and permeability development in synthetic salt rock. *Tectonophysics*. 1996;256:101–128. http://dx.doi.org/10.1016/0040-1951(95)00170-0.

[41] Hangx SJT, Spiers CJ, Peach CJ. Mechanical behavior of anhydrite caprock and implications for CO_2 sealing capacity. *J. Geophys. Res.* 2010;115:B07402 http://dx.doi.org/10.1029/2009JB006954.

[42] Wolterbeek TKT, Peach CJ, Spiers CJ. Reaction and transport in wellbore interfaces under CO_2 storage conditions: Experiments simulating debonded cement–casing interfaces. *Int. J. Greenh. Gas Control.* 2013;19:519–529. http://dx.doi.org/10.1016/j.ijggc.2013.10.017.

[43] Yurtdas I, Peng H, Burlion N, Skoczylas F. Influences of water by cement ratio on mechanical properties of mortars submitted to drying. *Cem. Concr. Res.* 2006;36:1286–1293. http://dx.doi.org/10.1016/j.cemconres.2005.12.015.

[44] Terzaghi K. *Theoretical Soil Mechanics*. New York: J. Wiley; 1943.

[45] Fredrich JT, Evans B, Wong T-F. Micromechanics of the brittle to plastic transition in Carrara marble. *J. Geophys. Res. Solid Earth.* 1989; 94:4129–4145. http://dx.doi.org/10.1029/JB094iB04p04129.

[46] Wong T, Baud P. The brittle-ductile transition in porous rock: A review. *J. Struct. Geol.* 2012;44:25–53. http://dx.doi.org/10.1016/j.jsg.2012.07.010.

[47] Wong T, David C, Zhu W. The transition from brittle faulting to cataclastic flow in porous sandstones: Mechanical deformation. *J. Geophys. Res.* 1997;102:3009–3025. accessed August 15, 2014 http://onlinelibrary.wiley.com/doi/10.1029/96JB03281/full.

[48] Roscoe KH, Schofield AN, Wroth CP. On the yielding of soils. *Géotechnique*. 1958;8:22–53.

[49] Rutter EH, Glover CT. The deformation of porous sandstones; are Byerlee friction and the critical state line equivalent? *J. Struct. Geol.* 2012;44:129–140.

[50] Curran JH, Carroll MM. Shear stress enhancement of void compaction. *J. Geophys. Res. Solid Earth.* 1979;84:1105–1112. http://dx.doi.org/10.1029/JB084iB03p01105.

[51] Zhu W, Baud P, Wong T. Micromechanics of cataclastic pore collapse in limestone. *J. Geophys. Res. Solid Earth.* 2010;115.

[52] Drucker DC, Prager W. Soil mechanics and plastic analysis or limit design. *Q. Appl. Math.* 1952;10:157–165.

[53] Davis RO, Selvadurai APS. *Plasticity and Geomechanics*. Cambridge University Press; 2002.

[54] Hsu TTC, Slate FO. Tensile bond strength between aggregate and cement paste or mortar. In: *ACI J. Proc.*. ACI; 1963.

[55] Pariseau WG. *Design Analysis in Rock Mechanics*. CRC Press; 2011.

[56] Zhu W, Baud P, Vinciguerra S, Wong T. Micromechanics of brittle faulting and cataclastic flow in Alban Hills tuff. *J. Geophys. Res. Solid Earth.* 2011;116.

[57] Baud P, Schubnel A, Wong T. Dilatancy, compaction, and failure mode in Solnhofen limestone. *J. Geophys. Res. Solid Earth.* 2000;105: 19289–19303.

[58] Timoshenko SP, Goodier JN. *Theory of Elasticity*. second ed. New York: McGraw Hill; 1951.

[59] Vajdova V, Baud P, Wong T. Compaction, dilatancy, and failure in porous carbonate rocks. *J. Geophys. Res. Solid Earth.* 2004;109.

[60] Swamy RN. Dynamic Poisson's ratio of portland cement paste, mortar and concrete. *Cem. Concr. Res.* 1971;1:559–583.

[61] Baud P, Vajdova V, Wong T. Shear-enhanced compaction and strain localization: Inelastic deformation and constitutive modeling of four porous sandstones. *J. Geophys. Res.* 2006;111:B12401 http://dx.doi.org/10.1029/2005JB004101.

[62] Stefanou I, Sulem J. Chemically induced compaction bands: Triggering conditions and band thickness. *J. Geophys. Res. Solid Earth.* 2014; 119:880–899.

[63] Chang CF, Chen JW. Strength and elastic modulus of carbonated concrete. *ACI Mater. J.* 2005;102:315–321. http://dx.doi.org/10.14359/14710.

[64] Çolak A. A new model for the estimation of compressive strength of Portland cement concrete. *Cem. Concr. Res.* 2006;36:1409–1413. http://dx.doi.org/10.1016/j.cemconres.2006.03.002.

[65] Scherer GW, Kutchko BG, Thaulow N, Duguid A, Mook B. Characterization of cement from a well at Teapot Dome Oil Field: Implications for geological sequestration. *Int. J. Greenh. Gas Control.* 2011; 5:115–124. http://dx.doi.org/10.1016/j.ijggc.2010.06.010.

[66] Rimmelé G, Barlet-Gouédard V, Porcherie O, Goffé B, Brunet F. Heterogeneous porosity distribution in Portland cement exposed to CO_2-rich fluids. *Cem. Concr. Res.* 2008;38:1038–1048. http://dx.doi.org/10.1016/j.cemconres.2008.03.022.

[67] Kutchko BG, Strazisar BR, Huerta N, Lowry GV, Dzombak DA, Thaulow N. CO_2 reaction with hydrated class H well cement under geologic sequestration conditions: Effects of flyash admixtures. *Environ. Sci. Technol.* 2009;43:3947–3952. http://dx.doi.org/10.1021/es803007e.

[68] Huet BM, Prevost JH, Scherer GW. Quantitative reactive transport modeling of Portland cement in CO_2-saturated water. *Int. J. Greenh. Gas Control.* 2010;4:561–574. http://dx.doi.org/10.1016/j.ijggc.2009.11.003.

[69] Geloni C, Giorgis T, Battistelli A. Modeling of rocks and cement alteration due to CO_2 injection in an exploited gas reservoir. *Transp. Porous Media.* 2011;90:183–200. http://dx.doi.org/10.1007/s11242-011-9714-0.

[70] Raoof A, Nick HM, Wolterbeek TKT, Spiers CJ. Pore-scale modeling of reactive transport in wellbore cement under CO_2 storage conditions. *Int. J. Greenh. Gas Control.* 2012;11:S67–S77. http://dx.doi.org/10.1016/j.ijggc.2012.09.012.

[71] Hangx SJT, van der Linden A, Marcelis F, Liteanu E. Defining the brittle failure envelopes of individual reaction zones observed in CO_2-exposed wellbore cement. *Environ. Sci. Technol.* 2015;50: 1031–1038. http://dx.doi.org/10.1021/acs.est.5b03097.

[72] Li Q, Lim YM, Flores KM, Kranjc K, Jun Y-S. Chemical reactions of portland cement with aqueous CO_2 and their impacts on cement's mechanical properties under geologic CO_2 sequestration conditions. *Environ. Sci. Technol.* 2015;49:6335–6343. http://dx.doi.org/10.1021/es5063488.

[73] Fabbri A, Corvisier J, Schubnel A, Brunet F, Goffé B, Rimmele G, et al. Effect of carbonation on the hydro-mechanical properties of Portland cements. *Cem. Concr. Res.* 2009;39:1156–1163.

[74] Smith DM, Scherer GW, Anderson JM. Shrinkage during drying of silica gel. *J. Non-Cryst. Solids.* 1995;188:191–206.

[75] Jung HB, Kabilan S, Carson JP, Kuprat AP, Um W, Martin P, et al. Wellbore cement fracture evolution at the cement–basalt caprock interface during geologic carbon sequestration. *Appl. Geochem.* 2014; 47:1–16. http://dx.doi.org/10.1016/j.apgeochem.2014.04.010.

[76] Jung HB, Um W. Experimental study of potential wellbore cement carbonation by various phases of carbon dioxide during geologic carbon sequestration. *Appl. Geochem.* 2013;35:161–172.

[77] Kampman N, Burnside NM, Shipton ZK, Chapman HJ, Nicholl JA, Ellam RM, et al. Pulses of carbon dioxide emissions from intracrustal faults following climatic warming. *Nat. Geosci.* 2012;5:352–358. http://dx.doi.org/10.1038/ngeo1451.

[78] Jaeger J, Cook NG, Zimmerman RW. *Fundamentals of Rock Mechanics*. fourth ed. Blackwell Publishing; 2007.

[79] Verberne BA, He C, Spiers CJ. Frictional properties of sedimentary rocks and natural fault gouge from the Longmen Shan fault zone, Sichuan, China. *Bull. Seismol. Soc. Am.* 2010;100:2767–2790.

[80] Chen J, Verberne BA, Spiers CJ. Interseismic re-strengthening and stabilization of carbonate faults by "non-Dieterich" healing under hydrothermal conditions. *Earth Planet. Sci. Lett.* 2015;423:1–12. http://dx.doi.org/10.1016/j.epsl.2015.03.044.

[81] Barclay I, Pellenbarg J, Tettero F, Pfeiffer J. The beginning of the end: a review of abandonment and decommissioning practices. *Oilf. Rev.* 2001;28–41. accessed August 18, 2014 http://www.slb.com/~/media/Files/resources/oilfield_review/ors01/win01/p28_41.pdf.

[82] Dusseault MB, Media P, Malcolm N. SPE 64733 why oilwells leak?: Cement behavior and long-term consequences, 2000.

[83] Jackson RE, Dusseault MB. Gas release mechanisms from energy wellbores, ARMA 14-7753. 2014.

[84] Thiercelin M, Dargaud B, Baret JF, Rodriquez WJ. Cement design based on cement mechanical response. *SPE Annu. Tech.* 1997; 266–273. accessed August 18, 2014 https://www.onepetro.org/conference-paper/SPE-38598-MS.

[85] Ravi K, Bosma M, Gastebled O. SPE 75700 safe and economic gas wells through cement design for life of the well, SPE 75700. 2002.

[86] ter Heege JH, Orlic B, Hoedeman GC. Characteristics of mechanical wellbore failure and damage: Insights of discrete element modelling and application to CO_2 storage, ARMA 15-174, 2015.

[87] Bois A-P, Garnier A, Galdiolo G, Laudet J-B. Use of a mechanistic model to forecast cement-sheath integrity, SPE-139668-PA, 2012. http://dx.doi.org/10.2118/139668-PA.

[88] Saint-Marc J, Garnier A, Bois A-P. Initial state of stress: The key to achieving long-term cement-sheath integrity, 2008. http://dx.doi.org/10.2118/116651-MS.

[89] Jennings HM. Refinements to colloid model of CSH in cement: CM-II. *Cem. Concr. Res.* 2008;38:275–289.

[90] Alizadeh R, Beaudoin JJ, Raki L. Viscoelastic nature of calcium silicate hydrate. *Cem. Concr. Compos.* 2010;32:369–376.

[91] Bois A-P, Vu M-H, Ghabezloo S, Sulem J, Garnier A, Laudet J-B. Cement sheath integrity for CO 2 storage–An integrated perspective. *Energy Procedia*. 2013;37:5628–5641.

[92] Huerta NJ, Hesse MA, Bryant SL, Strazisar BR, Lopano C. Reactive transport of CO_2-saturated water in a cement fracture: Application to wellbore leakage during geologic CO_2 storage. *Int. J. Greenh. Gas Control.* 2015; http://dx.doi.org/10.1016/j.ijggc.2015.02.006.

[93] Daccord G, Craster B, Ladva H, Jones T, Manescu G. In: Nelson E, Guillot D, eds. *Cement-Formation Interactions*. second ed. Schlumberger, Sugar Land, USA: Well Cem.; 2006.

[94] Oyibo A, Radonjic M. Impact of physical and chemical mud contamination on cement-formation shear bond strength. In: *ASME 2014 33rd Int. Conf. Ocean. Offshore Arct. Eng.*. American Society of Mechanical Engineers; 2014: V005T11A023–V005T11A023.

[95] Lecampion B, Quesada D, Loizzo M, Bunger A, Kear J, Deremble L, et al. Interface debonding as a controlling mechanism for loss of well integrity: Importance for CO_2 injector wells. *Energy Procedia*. 2011; 4:5219–5226. http://dx.doi.org/10.1016/j.egypro.2011.02.500.

[96] Lecampion B, Bunger A, Kear J, Quesada D. Interface debonding driven by fluid injection in a cased and cemented wellbore: Modeling and experiments. *Int. J. Greenh. Gas Control.* 2013;18: 208–223. http://dx.doi.org/10.1016/j.ijggc.2013.07.012.

[97] Newell DL, Carey JW. Experimental evaluation of wellbore integrity along the cement-rock boundary. *Environ. Sci. Technol.* 2012;47: 276–282.

[98] Carey JW, Svec R, Grigg R, Zhang J, Crow W. Experimental investigation of wellbore integrity and CO 2–brine flow along the casing–cement microannulus. *Int. J. Greenh. Gas Control.* 2010;4: 272–282.